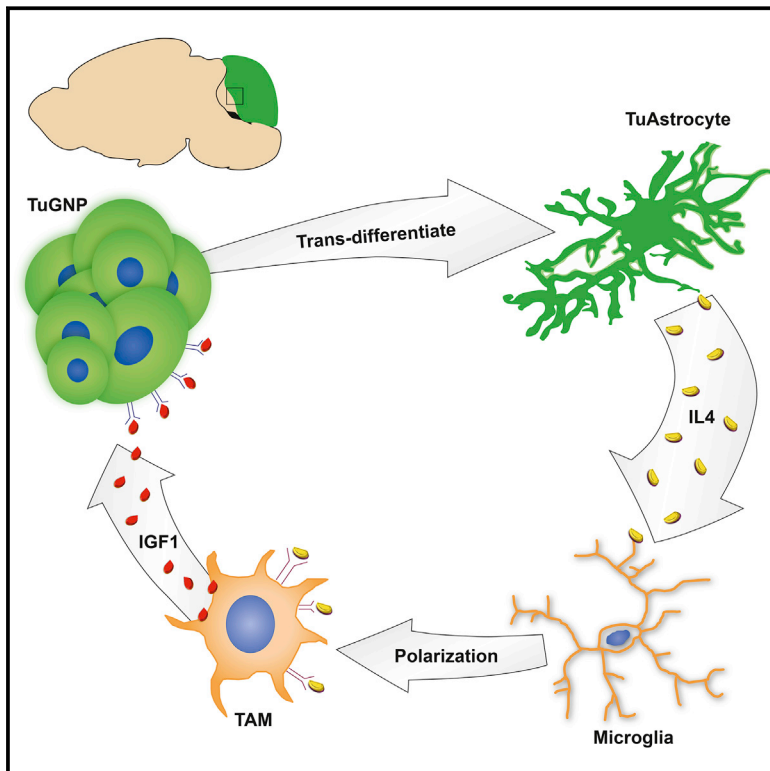


# Astrocytic *trans*-Differentiation Completes a Multicellular Paracrine Feedback Loop Required for Medulloblastoma Tumor Growth

## Graphical Abstract



## Authors

Maojin Yao, P. Britten Ventura, Ying Jiang, ..., Kevin A. Janes, Charles G. Eberhart, Hui Zong

## Correspondence

hz9s@virginia.edu

## In Brief

Tumors shape a microenvironmental network by acting as a source of tumor-associated astrocytes that provide paracrine stimulation to microglia to secrete IGF1, which is critical for tumor progression in SHH-activated mouse medulloblastoma models.

## Highlights

- A small number of medulloblastoma cells *trans*-differentiated into TME astrocytes
- Astrocytes in human SHH-subtype medulloblastoma share lineage with tumor cells
- Tumor-derived astrocytes secrete IL-4 to polarize microglia for IGF1 production
- IGF1 from tumor associated microglia is critical for tumor progression



# Astrocytic *trans*-Differentiation Completes a Multicellular Paracrine Feedback Loop Required for Medulloblastoma Tumor Growth

Maojin Yao,<sup>1,10</sup> P. Britten Ventura,<sup>1,10</sup> Ying Jiang,<sup>1,10</sup> Fausto J. Rodriguez,<sup>4</sup> Lixin Wang,<sup>2</sup> Justin S.A. Perry,<sup>1,11</sup> Yibo Yang,<sup>1</sup> Kelsey Wahl,<sup>5</sup> Rowena B. Crittenden,<sup>1,3</sup> Mariko L. Bennett,<sup>6,12</sup> Lin Qi,<sup>7</sup> Cong-Cong Gong,<sup>8</sup> Xiao-Nan Li,<sup>7,13</sup> Ben A. Barres,<sup>6</sup> Timothy P. Bender,<sup>1,3</sup> Kodi S. Ravichandran,<sup>1,3,9</sup> Kevin A. Janes,<sup>2</sup> Charles G. Eberhart,<sup>4</sup> and Hui Zong<sup>1,14,\*</sup>

<sup>1</sup>Department of Microbiology, Immunology, and Cancer Biology, University of Virginia, Charlottesville, VA 22908, USA

<sup>2</sup>Department of Biomedical Engineering, University of Virginia, Charlottesville, VA 22908, USA

<sup>3</sup>Beirne B. Carter Center for Immunology Research, University of Virginia, Charlottesville, VA 22908, USA

<sup>4</sup>Division of Neuropathology, Department of Pathology, Johns Hopkins University School of Medicine, Baltimore, MD 21205, USA

<sup>5</sup>Department of Biology, University of Oregon, Eugene, OR 97403, USA

<sup>6</sup>Department of Neurobiology, Stanford University, Palo Alto, CA 94305, USA

<sup>7</sup>Brain Tumor Program, Texas Children's Cancer Center, Department of Pediatrics, Baylor College of Medicine, Houston, TX 77030, USA

<sup>8</sup>School of Food Science and Engineering, South China University of Technology, Guangzhou, China

<sup>9</sup>VIB-UGent Center for Inflammation Research and Department of Biomedical Molecular Biology, Ghent University, Ghent, Belgium

<sup>10</sup>These authors contributed equally

<sup>11</sup>Present address: Immunology Program, Sloan Kettering Institute, Memorial Sloan Kettering Cancer Center, New York, NY 10065, USA

<sup>12</sup>Present address: Department of Pediatrics, Children's Hospital of Philadelphia, Philadelphia, PA 19104, USA

<sup>13</sup>Present address: Program of Precision Medicine PDOX Modeling of Pediatric Tumors, Ann and Robert H. Lurie Children's Hospital of Chicago and Department of Pediatrics, Northwestern University Feinberg School of Medicine, Chicago, IL 60611, USA

<sup>14</sup>Lead Contact

\*Correspondence: [hz9s@virginia.edu](mailto:hz9s@virginia.edu)

<https://doi.org/10.1016/j.cell.2019.12.024>

## SUMMARY

The tumor microenvironment (TME) is critical for tumor progression. However, the establishment and function of the TME remain obscure because of its complex cellular composition. Using a mouse genetic system called mosaic analysis with double markers (MADMs), we delineated TME evolution at single-cell resolution in sonic hedgehog (SHH)-activated medulloblastomas that originate from unipotent granule neuron progenitors in the brain. First, we found that astrocytes within the TME (TuAstrocytes) were *trans*-differentiated from tumor granule neuron precursors (GNPs), which normally never differentiate into astrocytes. Second, we identified that TME-derived IGF1 promotes tumor progression. Third, we uncovered that insulin-like growth factor 1 (IGF1) is produced by tumor-associated microglia in response to interleukin-4 (IL-4) stimulation. Finally, we found that IL-4 is secreted by TuAstrocytes. Collectively, our studies reveal an evolutionary process that produces a multi-lateral network within the TME of medulloblastoma: a fraction of tumor cells *trans*-differentiate into TuAstrocytes, which, in turn, produce IL-4 that stimulates microglia to produce IGF1 to promote tumor progression.

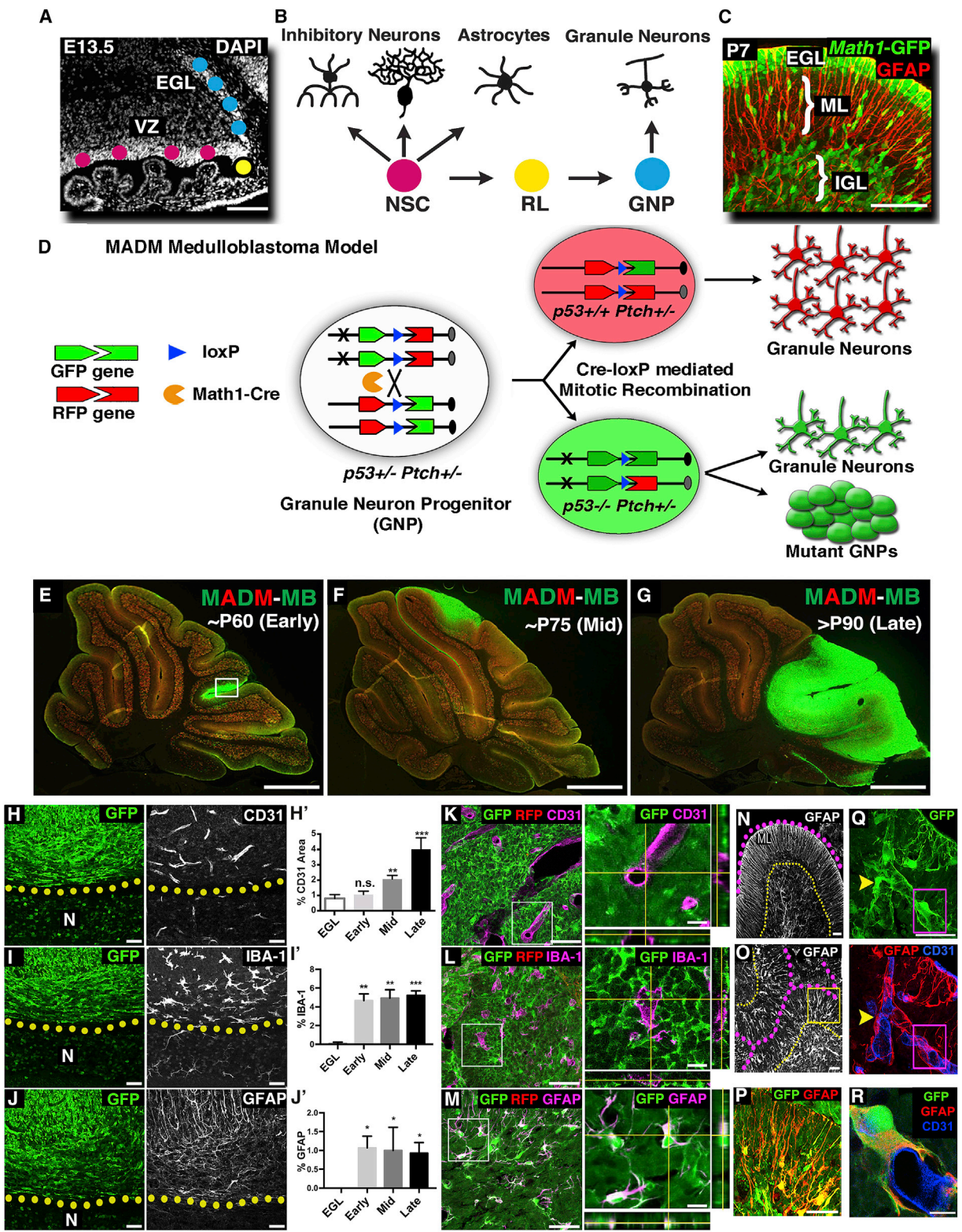
## INTRODUCTION

A tumor is a living organ. Cancer cells actively interact with the tumor microenvironment (TME) at multiple levels of complexity

for their survival (Balkwill et al., 2012; Hanahan and Coussens, 2012; Quail and Joyce, 2013). First, the TME consists of multiple cell types, including blood vessels (Chung et al., 2010; Folkman, 1971), fibroblasts (Gascard and Tlsty, 2016; Kalluri, 2016; Shiga et al., 2015), immune cells (Binnewies et al., 2018; de Visser et al., 2006; Gajewski et al., 2013), and other tissue-resident cells (Tabuso et al., 2017). Second, TME cells crosstalk among themselves to form a supportive environment for tumor cells (DeNardo et al., 2009; Gabriilovich et al., 2012; Kumar et al., 2018; Stockmann et al., 2014). Finally, the TME dynamically co-evolves with tumor cells from initiation to progression and full malignancy (Polyak et al., 2009; Weinberg, 2008). The TME can even be reprogrammed during cancer therapy and contribute to therapeutic resistance (Ahmed and Haass, 2018; Shee et al., 2018; Straussman et al., 2012; Su et al., 2018; Sun, 2016). Therefore, it is imperative to deconstruct the complexity of the TME: how a heterogeneous TME is established and how the crosstalk between TME cells supports tumor progression.

Although histopathological analyses of patient samples can reveal TME composition and correlation with prognosis, animal models are needed to delineate the origin of each TME component and provide mechanistic insights into TME functions (Arina et al., 2016; Özdemir et al., 2014; Wyckoff et al., 2004). To maximize the temporospatial resolution of TME analysis, our lab developed a mouse genetic system termed mosaic analysis with double markers (MADMs) (Zong et al., 2005). From a heterozygous mouse, MADMs relies on Cre-loxP-guided inter-chromosomal mitotic recombination to generate sparse green fluorescent protein (GFP)-labeled cells homozygous null for a given tumor suppressor gene (TSG) and red fluorescent protein (RFP)-labeled wild-type (WT) sibling cells in somatic tissues. The rarity of TSG-null cells, resulting from low efficiency of





(legend on next page)

recombination between two homologous chromosomes, not only mimics the clonal origin of cancer in human patients but also provides an unprecedented resolution for phenotypic analysis, and the immediate labeling of TSG mutant cells enables one to track them throughout the entire tumorigenic process (Liu et al., 2011). Careful choice of a Cre transgene that specifically expresses in tumor but not TME cells would allow one to investigate the recruitment, activation, and organization of non-labeled TME cells in relation to GFP-labeled tumor cells from tumor initiation to full malignancy.

Medulloblastoma is the most common malignant pediatric brain tumor, arising in the developing cerebellum (Gilbertson and Ellison, 2008), and the sonic hedgehog (SHH)-activated subtype contains multiple TME cell types (Bailey and Cushing, 1925; Wright, 1910), including neurons, endothelial cells, microglia-macrophages, and astrocytes (Figures S1A and S1B). Intriguingly, although medulloblastoma cells proliferate uncontrollably *in vivo*, propagating them *in vitro* has been very difficult, requiring serial transplantation in the brains of immunodeficient mice to expand human medulloblastoma cells (Shu et al., 2008). A potential explanation for this apparent paradox is that medulloblastoma cells rely on supportive signals from TME cells that are absent *in vitro*. In fact, the presence of an astrocytic component in medulloblastoma has been linked to poor prognosis even though its origin is unclear (Rickert and Paulus, 2005).

In addition to the clinical importance, studying the TME in the SHH subtype of medulloblastoma, which has an ostensibly simple tumor organization, could provide critical proof-of-principle groundwork. Years of research of this tumor type (Goodrich et al., 1997; Schüller et al., 2008; Yang et al., 2008) provide a vast amount of knowledge and well-characterized tools and techniques for this cancer type. First, the cell of origin for medulloblastoma, the granule neuron precursor (GNP), is a unipotent progenitor that does not give rise to any other cell types but granule neurons (Figures 1A–1C) (Zhang and Goldman, 1996), allowing one to use granule neuron precursor (GNP)-specific Math1-Cre (Matei et al., 2005) to mutate and label tumor but not TME cells

in a mouse model. Second, tumor GNPs can be specifically labeled by the Math1-GFP reporter transgene (Rose et al., 2009) to facilitate *in vivo* analysis and can be highly purified through Percoll gradient centrifugation for *in vitro* analysis (Oliver et al., 2005). Third, genetic mutations contributing to this tumor type have been well studied; heterozygous *Ptch1* mutation leads to upregulation of SHH signaling and significant tumor risks (Goodrich et al., 1997; Mullor et al., 2002; Pietsch et al., 1997), and *p53* loss results in a precipitous survival rate in human patients (Tabori et al., 2010) and shortened latency with full penetrance of tumor formation in mouse models (Wetmore et al., 2001). Finally, the brain is an “immune-privileged” organ in which microglia are the elementary tissue-resident macrophages and brain-specific astrocytes serve as non-professional immune cells (Burda and Sofroniew, 2014; Colombo and Farina, 2016; Prinz et al., 2017), providing a relatively simple system to decipher the interactions among cell types. As a tumor progresses, if blood-derived immune cells infiltrate into the tumor mass, as in neurological diseases or brain infections (Harris et al., 2012; Høglund and Maghazachi, 2014), then they can be readily identified for further functional studies. Here we created a MADM-based model for medulloblastoma with which we discovered an intricate TME network formed through *trans*-differentiation and multilateral paracrine signaling.

## RESULTS

### Establishment of MADM-Based and Other Genetic Models for Medulloblastoma

To pinpoint the contributions of diverse TME cells to the SHH-activated subtype of medulloblastoma (hereafter referred to as medulloblastoma), we established a MADM-based genetic model in which sporadic *Ptch1*-heterozygous, *p53*-null, GFP<sup>+</sup> GNPs were generated by Math1-Cre (Matei et al., 2005) in an otherwise *Ptch1*-heterozygous, *p53*-heterozygous mouse (Figure 1D). We chose Math1-Cre because it faithfully labels GNPs (Yang et al., 2008) (Figure S1C) but not potential TME cell types (Figure S1D), enabling us to investigate the establishment and

### Figure 1. MADM-Based Medulloblastoma Model Reveals that Some Tumor GNPs *trans*-Differentiate into Astrocytes

(A) The cerebellum develops from two physically separated progenitor pools: multipotent NSCs in the ventricular zone (VZ) and unipotent GNPs in the external granule layer (EGL).

(B) While NSCs give rise to inhibitory neurons and astrocytes, GNPs only give rise to granule neurons.

(C) At neonatal age, GNPs (Math1-GFP<sup>+</sup>) proliferate exponentially in the EGL, migrate along radial processes of Bergmann glia (GFAP<sup>+</sup>) in the molecular layer (ML) into the inner granule layer (IGL), and terminally differentiate into mature granule neurons.

(D) MADM-based medulloblastoma model that generates RFP<sup>+</sup>, *p53*<sup>+/+</sup> and GFP<sup>+</sup>, *p53*<sup>-/-</sup> GNPs in a *Ptch1*<sup>+/-</sup> mouse.

(E–G) The MADM-based medulloblastoma model had relatively consistent tumor progression kinetics: relatively small tumors around P60 (E), medium-sized tumors around P75 (F), and large tumors after P90 (G).

(H and I) Tumor-associated vessels had larger lumen sizes than adjacent normal tissue (N). Compared with the normal EGL, blood vessel coverage gradually increased as tumors progressed (n = 3, 4, 4, and 3, respectively).

(I and I') Microglia are few in the EGL but significantly increase during tumor progression (n = 3 each).

(J and J') Astrocyte cell bodies are absent in the EGL but significantly present in the tumor mass (n = 3 each).

(K–M), Blood vessels (K) and microglia (L) did not express GFP. In stark contrast, all GFAP<sup>+</sup> cells within the tumor mass (M) were GFP<sup>+</sup> (see also Video S1).

(N) In the normal cerebellum, GFAP<sup>+</sup> Bergmann glia extend radial processes through the ML (outlined with dotted lines).

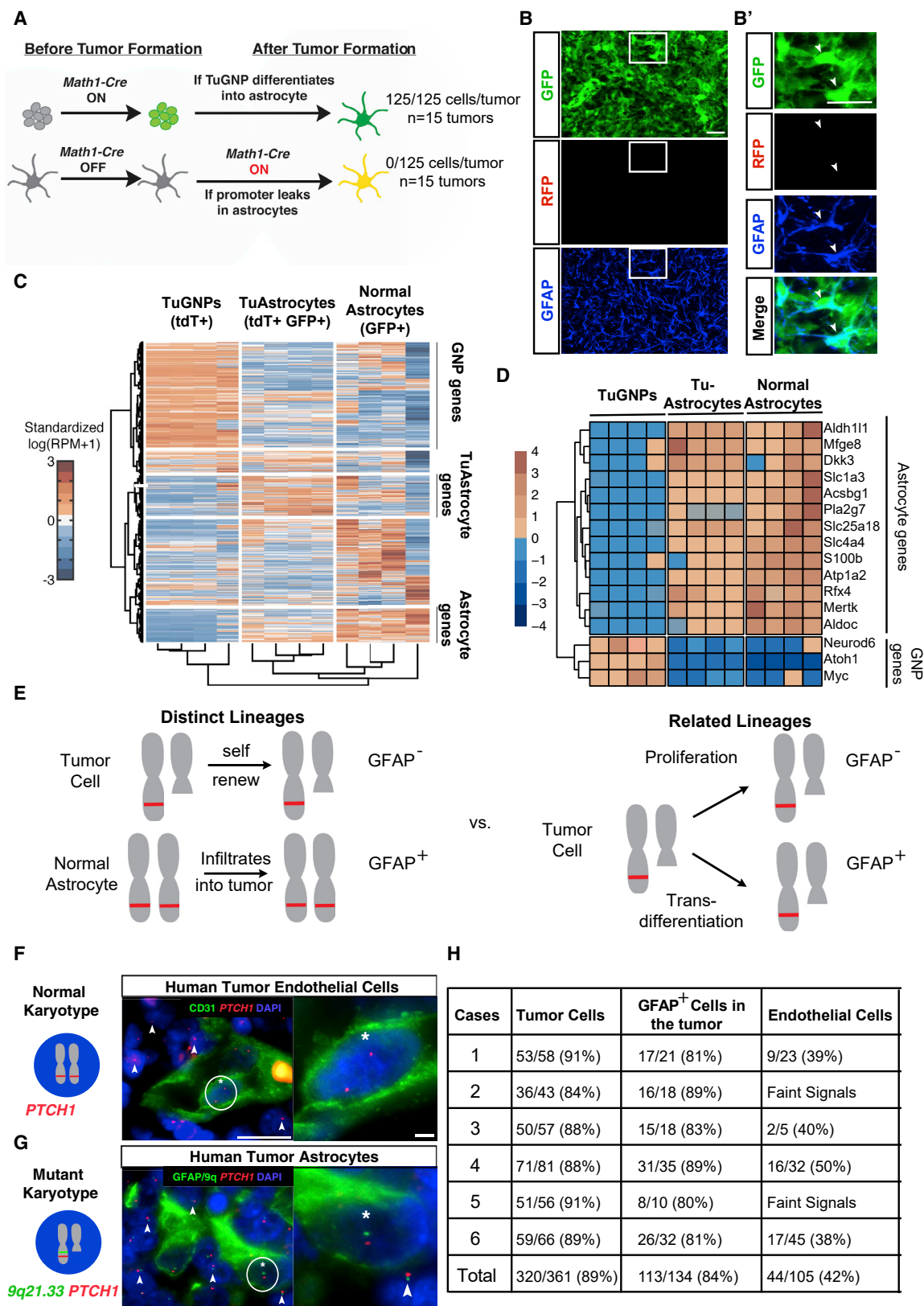
(O) A similar radial organization of GFAP<sup>+</sup> processes could be found in focal areas in the tumor mass (outlined with dotted lines).

(P) Higher magnification of the boxed region in (O).

(Q and R) Tumor-derived astrocytes (GFP<sup>+</sup>GFAP<sup>+</sup>) intimately interacted with blood vessels (CD31<sup>+</sup>), often wrapping an entire vessel (R; higher magnification of the boxed region in Q).

Scale bars are as follows: (A), 100 μm; (C), 50 μm; (E)–(G), 500 μm; (H)–(J) and (K)–(M) (left), (N), and (P), 50 μm; (K)–(M) (right), (Q) and (R), 10 μm. Data are mean ± SD. One-way ANOVA; n.s., not significant; \*p < 0.05, \*\*p < 0.01, \*\*\*p < 0.001.

See also Figure S1.



(legend on next page)

evolution of the TME throughout tumorigenesis (Figures 1E–1G; illustrated in Figure S1E).

In addition to the MADM-based model (Table S1, model A), three slightly modified mouse models were used in this study to address specific questions. In model B, *Math1-Cre* and a Cre reporter (Madisen et al., 2010) were used to specifically inactivate genes in GNPs and keep track of tumor lineage even after they differentiate into other cell types. In model C, *Math1-GFP* (Rose et al., 2009) was used as tumor cell marker to distinguish them from TME cells, and in model D, a Cre-free medulloblastoma model allowed us to designate Cre activity at desired times or in desired TME cell types for functional analysis. All of these are genetic models with an intact immune system and are free of injury-related complications common in tumor-grafting models.

### Progressive Accumulation of TME Cells as a Tumor Progresses and Discovery of *trans*-Differentiation of Astrocyte-like Cells from Tumor Cells

Immunofluorescence-based histological analysis of tumor sections at various stages from the MADMs model revealed that all types of TME cells observed in human medulloblastoma are abundantly present (Figures 1H–1J). Interestingly, distinct TME cells progressed at different rates; although the coverage of CD31<sup>+</sup> endothelial cells gradually increased as tumors progressed (Figure 1H), both IBA-1<sup>+</sup> tumor-associated microglia or macrophages (TAMs) and glial fibrillary acidic protein (GFAP)<sup>+</sup> astrocytes were drastically elevated at tumor onset and then remained at a constant composition throughout (Figures 1I' and J'). Because microglia and astrocytes are minimally present in the normal external granule layer (EGL), where tumor initiates (Figures 1I' and J', first bar), their sudden and abundant presence in even the smallest tumors implies their critical importance for malignancy. Finally, compared with normal brain regions (Figures 1H–1J and 1N), the enlarged vessel lumen (Figure 1H), reduced ramification of IBA-1<sup>+</sup> cells (Figure 1I), and elevated GFAP<sup>+</sup> expression (Figure 1J) in tumor regions collectively imply that these TME cells co-evolve with tumor cells.

To investigate the tumor-TME interactions, we closely examined the distribution of TME cells among GFP<sup>+</sup> tumor GNPs (referred to as TuGNPs hereafter) (Figures 1K–1M). We observed intermixed patterns of a minor population of TME cells intimately associated with tumor cells. Although endothelial cells and TAMs lacked GFP labeling (Figures 1K and 1L), unexpectedly, all astrocytes (GFAP<sup>+</sup>) in the tumor mass were GFP<sup>+</sup> in every tumor examined (Figure 1M; Video S1). Because we confirmed that *Math1-Cre* faithfully labels GNPs but not astrocytes in

normal brains (Figure S1D), it suggests that the GFAP<sup>+</sup>GFP<sup>+</sup> cells in medulloblastoma are likely TuGNP-derived rather than normal astrocytes.

In addition to GFAP, another marker for astrocytes, brain lipid-binding protein (BLBP), also showed overlapped staining with GFP (Figures S1F and S1F'). Importantly, BLBP<sup>+</sup> GFP<sup>+</sup> cells were confined to the tumor region but never found in adjacent normal regions (Figure S1F' versus Figure S1F''), suggesting a tumor-specific phenomenon. To further examine the nature of these cells, we established a medulloblastoma model in which the GNP lineage is labeled with tdTomato (Table S1, model B) and astrocytes are labeled by an astrocyte-specific *Aldh1L1-GFP* bacterial artificial chromosome (BAC) transgene (Gong et al., 2003). The observed co-expression of GFP and tdTomato (Figure S1G) lent further support to the astrocytic nature of these TuGNP-derived cells. Finally, we also noted a remarkable morphological resemblance of these GFAP<sup>+</sup> cells to normal astrocytes. Phenocopying Bergmann glia in normal cerebellum (Figure 1N), a radial arrangement of GFP<sup>+</sup> GFAP fibers was highly evident at the edge of early- to mid-stage tumors (Figures 1O and 1P). Additionally, GFP-labeled astrocyte-like cells intimately associated with blood vessels throughout tumor regions (Figures 1Q and 1R), reminiscent of another salient feature of normal astrocytes (Abbott et al., 2006; Iadecola and Nedergaard, 2007). In summary, the cellular resolution provided by MADMs not only revealed the co-evolution process of TME cells during tumor progression but also led to an unexpected finding of potential *trans*-differentiation of TuGNPs to astrocytes.

### Validation of Astrocyte Identity of Cells *trans*-Differentiated from TuGNPs and Human Relevance

Although intrigued, we are acutely aware of alternative interpretations of the observed *trans*-differentiation. One possibility is promoter leakage. Although *Math1-Cre* faithfully labels GNPs in the normal brain, the *Math1* promoter could be mis-activated in astrocytes after they are recruited into the tumor mass. Although this possibility cannot be ruled out by conventional Cre reporters, it was readily excluded by the dual-color design of MADMs because promoter leakage would result in yellow astrocytes (illustrated in Figure 2A), which were never observed in all tumors (Figures 2B and 2B'). The possibility of cell fusion between astrocytes and GFP-labeled TuGNPs was ruled out because we never observed binucleated cells after examining more than 1,000 BLBP<sup>+</sup>GFP<sup>+</sup> cells from 10 individual tumors (Figure S2A). Just in case nuclei fused after cell fusion, resulting in single-nucleus fused cells, we

#### Figure 2. Validation of Tumor-to-Astrocyte *trans*-Differentiation

- (A) Schematic explanation of how the MADMs system could definitively rule out the “Cre leakage” interpretation.  
 (B and B') Representative images from the MADMs model, showing that GFAP<sup>+</sup> cells are not yellow.  
 (C) Hierarchical clustering of RNA-seq data for TuGNPs, normal astrocytes, and TuAstrocytes.  
 (D) Many astrocytic markers are elevated in TuAstrocytes, whereas signature TuGNP genes are decreased in TuAstrocytes.  
 (E) Schematic illustration of how karyotypic analysis of astrocytes in human medulloblastoma could reveal their lineage relationship with tumor cells.  
 (F) Endothelial cells (CD31<sup>+</sup>) have a normal karyotype (two red FISH signals, the cell marked with an asterisk is magnified on the right), whereas surrounding tumor cells have one red signal (arrowheads), indicating loss of one *PTCH1*-containing chromosomal fragment.  
 (G) Loss of one allele from the 9q21.33 region to the *PTCH1* locus was seen in GFAP<sup>+</sup> cells (the cell marked with an asterisk is magnified on the right), the same as surrounding tumor cells (arrowheads).  
 (H) Quantification showing that the majority of TuGNPs and TuAstrocytes in all six patient samples share the same karyotypic aberration.  
 Scale bars are as follows: (B) and (B'), 20 μm; (F) and (G) (left), 25 μm; (F) and (G) (right), 10 μm.  
 See also Figure S2.

established a medulloblastoma model in which all GNPs are labeled with GFP (Table S1, model D) and all astrocytes are labeled with tdTomato (Figure S2B) to capture events based on the generation of yellow cells (illustrated in Figure S2C). The fact that yellow TME astrocytes were never observed after examining more than 100 tdTomato<sup>+</sup> cells in 4 tumor-bearing mice (Figure S2D) definitively ruled out the possibility of cell fusion. Finally, we ruled out the possibility of GFP protein transfer from TuGNPs to astrocytes because in model C (Table S1), all astrocytes were GFP-negative even though all tumor cells were labeled by Math1-GFP (data not shown).

To pinpoint the identity of these “astrocyte-like” cells more definitively, we profiled their transcriptome using laser-capture microdissection (LCM) followed by RNA sequencing. To visualize target cells in the tumor mass without immunostaining, we used a mouse model in which TuGNPs are red, tumor-derived astrocyte-like cells are yellow, and normal astrocytes are green (Figure S2E, model B). After extensive optimization of the tissue-processing procedure to avoid diffusive loss of fluorescent proteins in unfixed tissue (Singh et al., 2019; Wang and Janes, 2013; Figure S2F; STAR Methods), we were able to visualize both GFP and tdTomato and collected ~250 astrocyte-like cells from each tumor sample. After extracting RNA, amplifying cDNA (Janes et al., 2010; Wang and Janes, 2013), and confirming the purity of LCM-collected astrocyte-like cells, TuGNPs, and normal cerebellar astrocytes (Figures S2G and S2H), we performed RNA sequencing followed by unsupervised clustering of transcriptomic profiles (n = 4 each). We found that astrocyte-like tumor cells clustered more closely to normal astrocytes than to TuGNPs (Figure 2C). Notably, almost all of the TuGNP-specific transcripts were downregulated in astrocyte-like cells (Figures 2C, top, and 2D, bottom), whereas many astrocyte-specific transcripts were upregulated (Figures 2C, bottom, and 2D, top), suggesting extensive *trans*-differentiation. Because the astrocyte-like cells closely resemble but still differ from normal astrocytes in ~2,500 uniquely expressed transcripts (Figure 2C, center), here we refer to them as “TuAstrocytes.”

Finally we investigated with two approaches whether the astrocytic component long recognized in human medulloblastomas (Burger et al., 1987; Mannoji et al., 1981; Figures S1A and S1B) was descended from TuGNPs. First we assessed whether patient-derived medulloblastoma cells could *trans*-differentiate into astrocytes in xenografts. To avoid culture-induced artifacts, we used a primary human SHH-subgroup medulloblastoma that has been serially xenografted into the brains of nonobese diabetic (NOD)/severe combined immunodeficiency (SCID) mice and authenticated by gene expression profiling along the passages (Shu et al., 2008; Zhao et al., 2012). We consistently observed human GFAP-specific immunoreactivity within all xenografted tumors examined (Figures S2I and S2J). Because these tumor cells had been grafted through multiple passages to eliminate non-tumor cells, these human GFAP<sup>+</sup> cells most likely were *trans*-differentiated from TuGNPs. For our second approach, we exploited the fact that the *PTCH1* locus on chromosome 9q in the human genome is recurrently lost in human desmoplastic medulloblastoma (Schofield et al., 1995). We predicted that, if astrocytes in the tumor were not lineage-related to tumor cells, then they would have a

normal karyotype (Figure 2E, left), whereas, if astrocytes are lineage-related to tumor cells, then astrocytes would have the identical chromosomal loss as surrounding tumor cells (Figure 2E, right). Among 21 cases of SHH-activated subtype human medulloblastoma, six were identified with 9q loss that warranted further study. We assessed the chromosomal integrity in each astrocyte within the tumor mass by two-color fluorescent *in situ* hybridization (FISH) for *PTCH1* (9q22.33) and an adjacent locus (9q21.33) along with immunofluorescent staining of GFAP. To ensure that these patients are not germline carriers for this karyotypic aberration, which would confound data interpretation, we verified that many endothelial cells in the tumor mass had a normal karyotype (Figure 2F). The fact that GFAP<sup>+</sup> cells had significant enrichment for monoallelic *PTCH1*-9q21.33 loss to the same level as tumor cells (Figure 2G) in six of six cases (summarized in Figure 2H) suggests that these astrocytes share a common lineage with tumor cells harboring the same genetic lesion.

After exhaustively examining all conceivable alternative interpretations, we concluded that TuAstrocytes in the TME are derived from TuGNPs in both mouse models and human medulloblastoma patients.

### TuAstrocytes Appear to Support Tumor Progression

To determine the function of TuAstrocytes, we first sought to determine whether TuAstrocytes display cancer stem cell characteristics because GFAP is a marker gene for not only astrocytes but also neural stem cells (Doetsch et al., 1999). Because the purification of viable TuAstrocytes was not feasible (data not shown), we established a mouse medulloblastoma model in which TuAstrocytes are labeled with RFP upon tamoxifen injection (Figure 3A, model D), with an expectation to find RFP<sup>+</sup> TuGNPs after an extended period if TuAstrocytes function as cancer stem cells. However, no red TuGNPs were observed 2 weeks after Tamoxifen injection (Figure 3B). In case more time was needed for TuAstrocytes to give rise to TuGNPs, we transplanted unlabeled primary tumors from this model into NOD-SCID mice, administered tamoxifen after tumors started growing, and waited 2 months. The fact that we still did not observe any RFP<sup>+</sup> TuGNPs (Figure 3C) does not support a cancer stem cell role of TuAstrocytes.

Next, we probed tumor-supporting roles of TuAstrocytes with two experiments. First, we examined the correlation between the presence of TuAstrocytes and the progression of pre-neoplastic lesions (PNLs) (Oliver et al., 2005), of which only some progress to full malignancy. After identifying PNLs on the surface of the cerebellum in *Ptch1*<sup>+/-</sup> mice at post-natal day 35 (P35), we assessed correlation between overall content of astrocytes and the proliferative status of GNPs (Figures S3A and S3B). Across more than 30 PNLs, we found that the presence of astrocytes strongly correlated with GNP proliferation and vice versa ( $p < 10^{-5}$ , Fisher's exact test; Figure S3C), suggesting that astrocytes might play important roles in PNL progression. Second, when purified TuGNPs were cultured *in vitro*, we observed that, although dispersed cells stopped proliferating quickly, those aggregating cells showed robust proliferation (Figure S3D). To investigate whether TuAstrocytes were involved, we prepared RFP<sup>+</sup> TuGNPs from the Aldh1L1-GFP model used for the LCM experiment (Figure S2E, model B). Although all cells were red initially, GFP<sup>+</sup> TuAstrocytes started to appear in aggregates as early as day 3 in culture

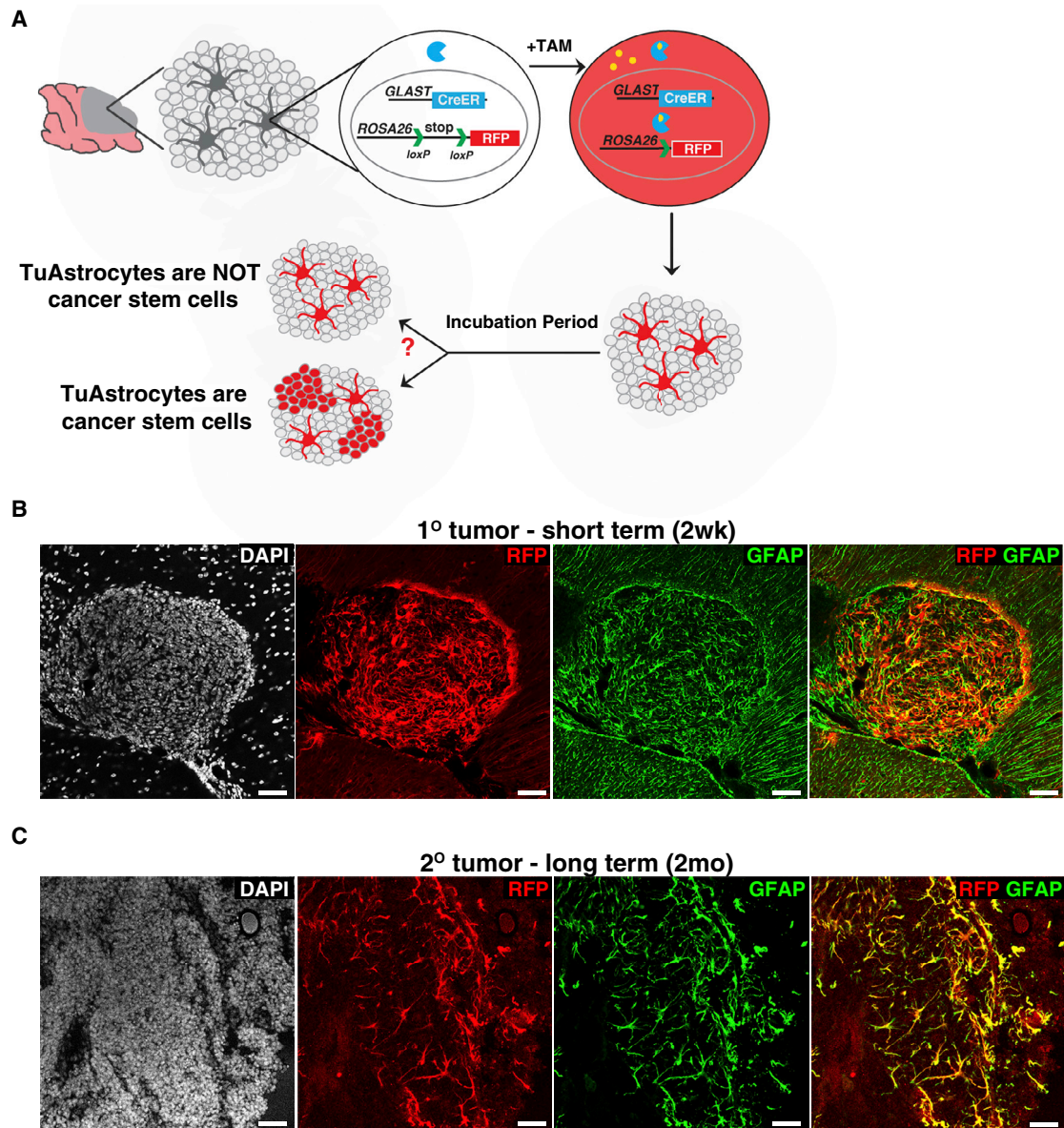


### Figure 3. TuAstrocytes Seem to Not Behave Like Cancer Stem Cells

(A) Schematic illustration of the mouse model and expected outcomes. (B) TuAstrocytes did not give rise to TuGNPs 2 weeks after tamoxifen injection. (C) TuAstrocytes did not give rise to TuGNPs, even after 2 months. Scale bars are as follows: (B) and (C), 50  $\mu\text{m}$ .

See also [Figure S3](#).

([Figures S3E and S3G](#)) and increased substantially by day 6 ([Figures S3F and S3G](#)), indicating concurrence between spontaneous TuGNP-to-TuAstrocyte *trans*-differentiation and sphere expansion in culture. Taken together, we conclude that TuAstrocytes are not cancer stem cells but, rather likely, play a supportive role regarding TuGNPs.

### IGF1 Is a Tumor-Supporting TME Factor

Next, we asked how TuAstrocytes might promote tumor progression by examining a panel of eight growth factors known

to be important for brain development and tumor progression. First we performed qRT-PCR to compare their expression levels in tumors and normal brains, hypothesizing that candidate factors should consistently be expressed at higher levels in tumors. We identified three candidate factors—insulin-like growth factor 1 (IGF1), hepatocyte growth factor (HGF), and platelet-derived growth factor A (PDGF-A)—that were consistently 2-fold or more higher in tumors ([Figure 4A](#)). To distinguish TME-derived from tumor-intrinsic factors, we performed paired qRT-PCR of these three factors between the tumor mass and purified



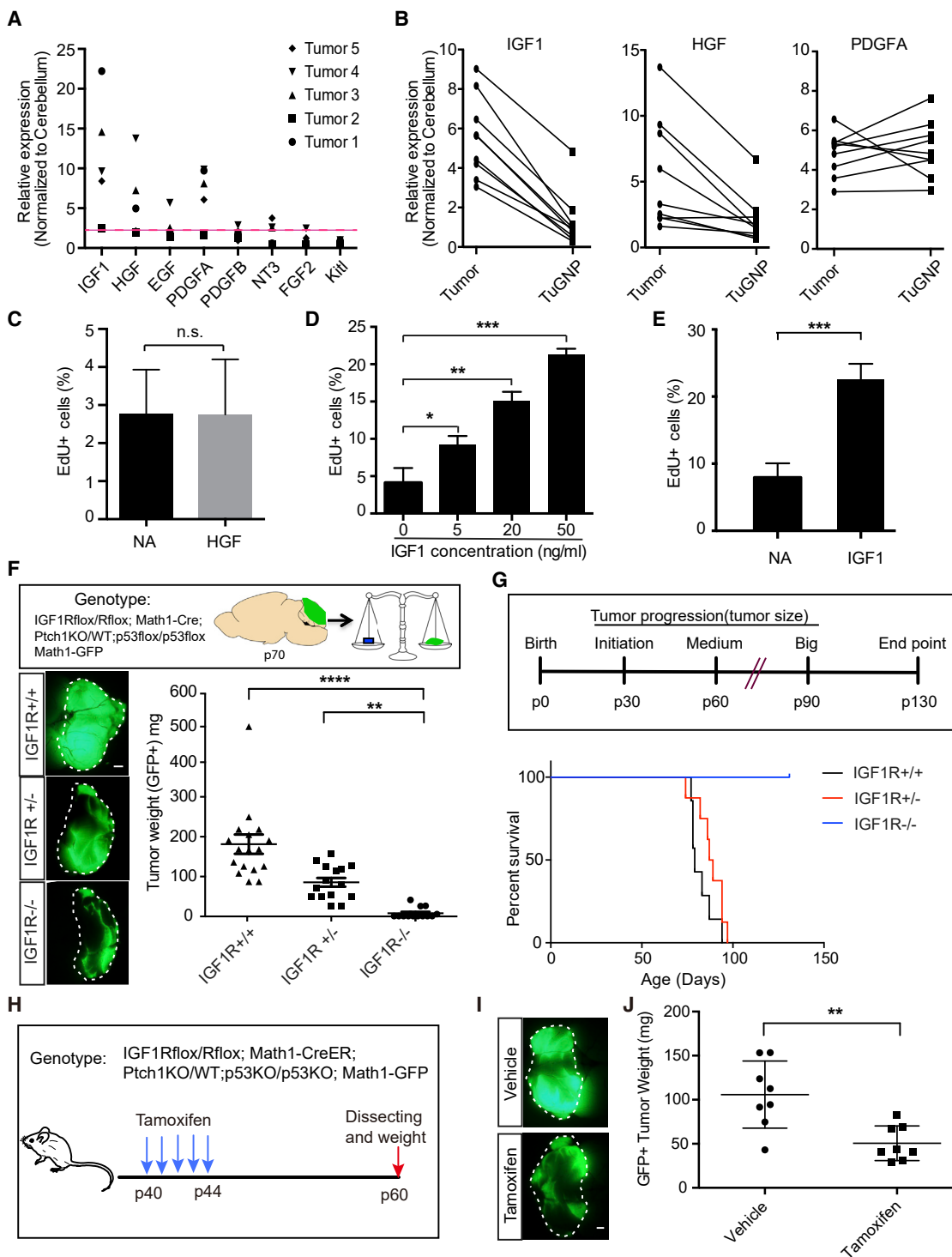


**Figure 4. IGF1 Is a TME Factor Necessary for Tumor Progression**

(A) Expression of growth factors in tumors in comparison with normal cerebellum.

(B) Expression levels of IGF1 and HGF, but not PDGF-A, were much higher in the tumor mass than in purified tumor GNPs (n = 8).

(C) HGF did not promote tumor cell proliferation.

(D and E) IGF1 promoted proliferation of both mouse (D) and human tumor cells (E).

(F) Inactivation of IGF1R in GNPs delayed tumor progression (n ≥ 12 for each genotype).

(legend continued on next page)

TuGNPs and found that IGF1 and HGF, but not PDGF-A, were TME-derived factors (Figure 4B). Next, we found that IGF1, but not HGF, promoted the proliferation of TuGNPs in cell culture in a dose-dependent manner (Figures 4C and 4D). Finally, the importance of IGF1 in human medulloblastoma was supported by IGF1-dependent proliferation of a human SHH medulloblastoma line (Shu et al., 2008; Zhao et al., 2012) (Figure 4E).

To determine whether IGF1 signaling is critical for medulloblastoma progression, which is well known for its reliance on Shh signaling (Goodrich et al., 1997; Mullor et al., 2002; Pietsch et al., 1997), we established a mouse model in which IGF1R is genetically deleted specifically in GNPs (Figure S4A, model C plus IGF1R-flox alleles, hereafter referred to as insulin growth factor 1 receptor-conditional knockout [IGF1R-CKO]). We found that IGF1R is critical for both tumor initiation (Figures S4B and S4C) and progression (Figure 4F) because tumor sizes were much smaller in IGF1R-CKO mice compared with the control group at both stages. IGF1R-CKO mice survived much longer than IGF1R-WT and IGF1R-heterozygous mice (Figure 4G). Histological examination of brains at the study endpoint (P130) revealed few tumor cells in IGF1R-CKO brains, indicating the indispensable role of IGF1R signaling in medulloblastoma. It should be noted that, because *Math1-Cre* is expressed throughout GNP development, the lack of tumor formation in this model could be caused by developmental defects of GNPs upon IGF1R inactivation. To rule out this possibility, we established another mouse model in which IGF1R deletion is mediated by tamoxifen-dependent *Math1-CreER* (Figure 4H, model D). After confirming that tamoxifen had no effect on tumor progression (Figure S4D), we injected tamoxifen to inactivate IGF1R in TuGNPs after tumor formation (P40). The reduction of tumor size in tamoxifen-treated mice in comparison with vehicle controls (Figures 4I and 4J) suggests that acute inactivation of IGF1 signaling in TuGNPs halted tumor progression. To probe the cause of the tumor size reduction, we further examined the apoptotic index and cell cycle exit index of TuGNPs (illustrated in Figure S4E) and found that IGF1R-null TuGNPs are much more likely to die and exit the cell cycle than IGF1R-WT TuGNPs (Figures S4F–S4I).

In summary, these data suggest that TME-derived IGF1 signaling is critical not only for initiation but also for sustained progression of medulloblastoma.

### IGF1 Is Secreted by TAMs Rather Than by TuAstrocytes

Because TuAstrocytes are *trans*-differentiated from TuGNPs, we established a complementary mouse model to inactivate *IGF1* with *Math1-Cre* (model C plus IGF1-flox alleles), expecting it to phenocopy the *IGF1R* knockout model. Surprisingly, the IGF1 knockout (KO) model failed to slow tumor progression, leading to our suspicion that TuAstrocytes might not be the cellular source of IGF1. Using RNA *in situ* hybridization to detect IGF1 and immunofluorescent staining to identify cell types, we found that IGF1 is specifically produced by IBA-1<sup>+</sup>

tumor-associated myeloid cells (TAMs) but not TuAstrocytes (Figures 5A and 5B). Interestingly, although ~70% of TAMs were IGF1<sup>+</sup>, no detectable IGF1 was seen in microglia in normal brain regions (normal versus tumor region, Figure 5A, center; quantified in Figure 5C). After affinity-based purification of TAMs and microglia, we further verified by qRT-PCR that the expression level of IGF1 is more than an order of magnitude greater in TAMs than in normal microglia (Figure 5D). Coculturing purified TAMs and TuGNPs showed that TAMs promoted TuGNP proliferation in a density-dependent manner (Figures 5E and 5F), which is IGF1-dependent because the IGF1-sequestering protein IGFBP3 (Ranke, 2015) completely abrogated the tumor-supporting activity of TAMs (Figure 5G, column 3 versus column 2). To investigate the role of TAM-secreted IGF1 *in vivo*, we established another medulloblastoma model in which *IGF1* is inactivated by myeloid-specific *CSF1R-Cre* (Deng et al., 2010; Figure 5H, model D). We found that TAM-specific deletion of IGF1 resulted in much smaller tumors at P35 compared with tumors under IGF1-WT conditions (Figures 5I and 5J, *n* > 10), suggesting a supportive role of IGF1 from TAMs in tumor initiation.

### TAMs Are Locally Activated Microglia and Not Circulating Monocyte-Derived Macrophages

Why do most TAMs but few normal microglia express IGF1? One possible explanation could be their distinct origins. Derived from the embryonic yolk sac and shaped by the brain environment, microglia are intrinsically different from macrophages derived from circulating monocytes (Ginhoux et al., 2010; Goldmann et al., 2016; Gomez Perdiguero et al., 2015; Gosselin et al., 2014). Therefore, the elevated IGF1 expression in TAMs could mean that TAMs originated from circulating-monocyte derived macrophages, especially because we noted that TAMs had morphologies highly distinct from resident microglia (Figures S5A–S5F). Our initial attempt to pinpoint the origin of TAMs based on their marker expression was unsuccessful because of its puzzling pattern. Although they stained positively for the microglia marker P2RY12 (Butovsky et al., 2014), they also expressed the monocyte-derived macrophage marker CCR2 (Kurihara et al., 1997; Siebert et al., 2000) (Figures S5G and S5H). Even more puzzling was the lack of expression of TMEM119 (Figure S5I), which has been shown previously to remain stable in microglia even in the presence of brain inflammation and injuries (Bennett et al., 2016). Although these efforts turned out to be inconclusive, they nevertheless revealed a strong influence of TME factors on TAM states.

Next, we turned to a lineage tracing method to distinguish microglia from monocyte-derived macrophages. Using this approach, initially labeled monocytes would be replaced by unlabeled monocytes derived from stem cells because of their fast turnover, but microglia would remain labeled because of slow and local replenishment (Figure 6A; Goldmann et al., 2013;

(G) Inactivation of IGF1R in GNPs prolonged mouse survival. Although all *IGF1R<sup>+/+</sup>* (*n* = 7) and *IGF1R<sup>-/+</sup>* (*n* = 8) tumor mice died before P90, all IGF1R-null mice (*n* = 14) survived until the experimental endpoint (P130).

(H) The medulloblastoma model in which IGF1R can be inactivated after tumor onset.

(I) Tamoxifen-induced (150 mg/kg) inactivation of IGF1R in tumor GNPs suppressed tumor progression (*n* = 8 for each group).

Scale bars are as follows: (F) and (I), 1 mm. Data are means ± SD. Student's *t* test (C–E) or one-way ANOVA (F and I); \*\**p* < 0.01, \*\*\**p* < 0.001, \*\*\*\**p* < 0.0001. See also Figure S4.

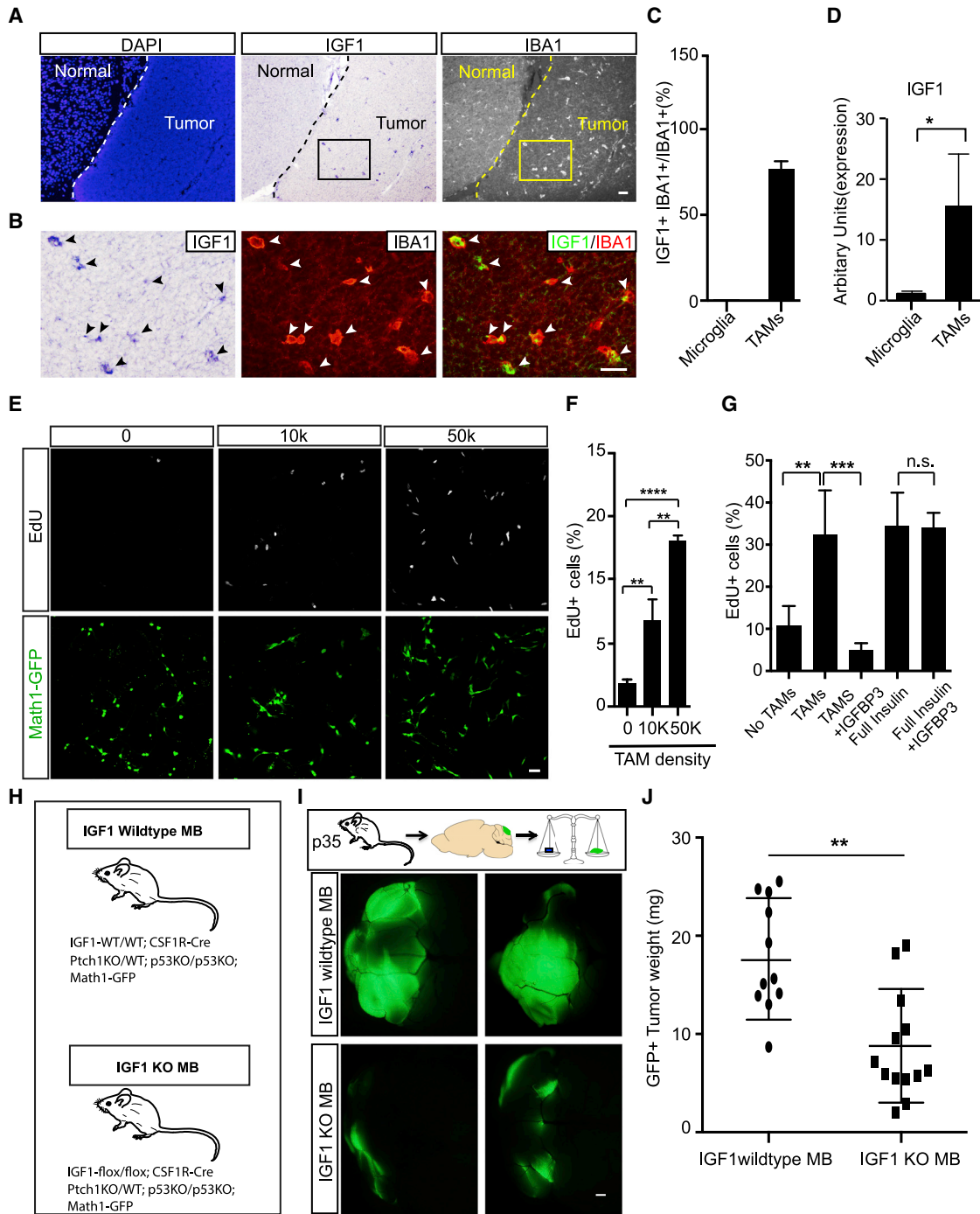


**Figure 5. IGF1 Produced by TAMs Is Critical for Tumor Progression**

(A and B) *In situ* hybridization showed that IGF1 was produced by IBA1<sup>+</sup> TAMs but not by normal microglia. Low magnification (A) and high magnification (B). (C) The proportion of IGF1-producing IBA1<sup>+</sup> TAMs (n = 4). (D) qRT-PCR comparison of IGF1 expression levels in acute purified microglia and TAMs. (E and F) Proliferation of tumor GNPs was enhanced by acutely purified TAMs in a density-dependent fashion. (G) TAM-promoted proliferation of tumor GNPs was abrogated by IGF1-blocking IGFBP3. General toxicity of IGFBP3 was ruled out by the fact that it could not block the proliferation of tumor GNPs induced by insulin, which activates IGF1R but cannot be blocked by IGFBP3. (H) Medulloblastoma mouse model with IGF1 KO in TAMs. (I and J) Representative images (I) and tumor weight (J) in *IGF1*<sup>-/-</sup> tumor mice (n = 13) and IGF1 WT controls (n = 11) at P35.

(legend continued on next page)

Yona et al., 2013). We carefully re-validated the system to rule out possible interference by genetic mutations in the medulloblastoma model (Figure S6). To avoid the slim possibility that monocytes labeled in early tumor lesions lodging in the tumor mass might fail to turn over, we injected tamoxifen at P7, long before tumor initiation. When we examined brain sections at P40, when tumors were still small, and at P60, when tumors fully developed, we found that all TAMs in the tumor mass were labeled by tdTomato, suggesting that they originated from the microglia (Figures 6B–6E). Complementary to the lineage tracing experiment, RNA sequencing (RNA-seq) analysis of purified TAMs followed by hierarchical cluster analysis also indicated that TAMs shared more transcriptomic similarity with microglia than with circulating monocyte-derived macrophages (Figures 6F and 6G). Notably, TAMs displayed significant alterations of gene expression compared with normal microglia and demonstrated even greater deviation from normal microglia than LPS-treated microglia (Figure 6G), suggesting that they were heavily shaped by local TME factors. Finally, in addition to microglia, one recent paper reported that meningeal macrophages also turn over slowly (Goldmann et al., 2016), which could also be a source of labeled TAMs. Dextran dye labeling of meningeal macrophages (Figures 6H and 6I) followed by 3 and 7 days of monitoring did not detect infiltration (Figures 6J and 6K) suggested that meningeal macrophages are unlikely to be a significant source of TAMs. Taken together, these data suggest that TAMs originate from microglia and undergo significant morphological and functional changes that are likely induced by TME factors.

#### IL-4 Signaling Is Responsible for Stimulating Increased IGF1 Expression by TAMs

Because TAMs originate from microglia that normally do not express high levels of IGF1, we pursued the hypothesis that IGF1 expression in TAMs is caused by alteration of their immune state induced by TME factors. We first performed comprehensive bioinformatic analysis of RNA-seq data of TAMs in comparison with normal microglia with a focus on tolerogenic signature genes (Chanmee et al., 2014) demonstrated previously to promote tumorigenesis (Noy and Pollard, 2014). Among 4,898 upregulated and 4,521 downregulated genes, we found an overall tolerogenic signature, including a bias toward IL-10 production, negative regulation of adaptive immunity, negative regulation of inflammatory responses, factors associated with Th2 immunity, and IL-4-mediated signaling events (Figure S7A).

Next, we examined two pathways that are best known for IGF1-induction in macrophages/microglia: IL-4 and tumor necrosis factor alpha (TNF- $\alpha$ ) (Fournier et al., 1995; Lake et al., 1994; Spadaro et al., 2017; Wynes and Riches, 2003). We found that genes in the IL-4 pathway are globally elevated in TAMs, especially those elicited in a STAT6-dependent manner (Figure 7A). In support of this finding, we observed a significant increase in differentially expressed genes regulated by IL-4-related kinases in macrophages, including JAK2 and ERK1-

ERK2 (Figure S7B). On the contrary, genes known to be elicited in macrophages stimulated with TNF- $\alpha$  were generally downregulated, including genes dependent on TNF- $\alpha$  signaling via nuclear factor  $\kappa$ B (NF- $\kappa$ B) and AP1 (Figure 7B, blue bars), whereas genes that are thought to be suppressed by TNF- $\alpha$  were upregulated (Figure 7B, red bar). These findings are in accordance with our Luminex profiling data, which indicated an increase in IL-4 but not TNF- $\alpha$  in the tumor mass (Figure 7C; Table S2). To investigate the functional relevance, we purified TAMs from the tumor mass and demonstrated a significant increase in IGF1 expression upon IL-4 stimulation (Figure 7D). In a complementary experiment, we established a mouse medulloblastoma model with an IL-4-null background (Figure S7C, model C). Although IL-4 KO did not alter the number of TAMs in the tumor mass (Figure 7E; Figure S7D), it led to a significant decrease in IGF1 expression in the tumor mass (Figure 7F). Therefore, this set of experiments indicated that IL-4 is sufficient and necessary to promote IGF1 expression in TAMs.

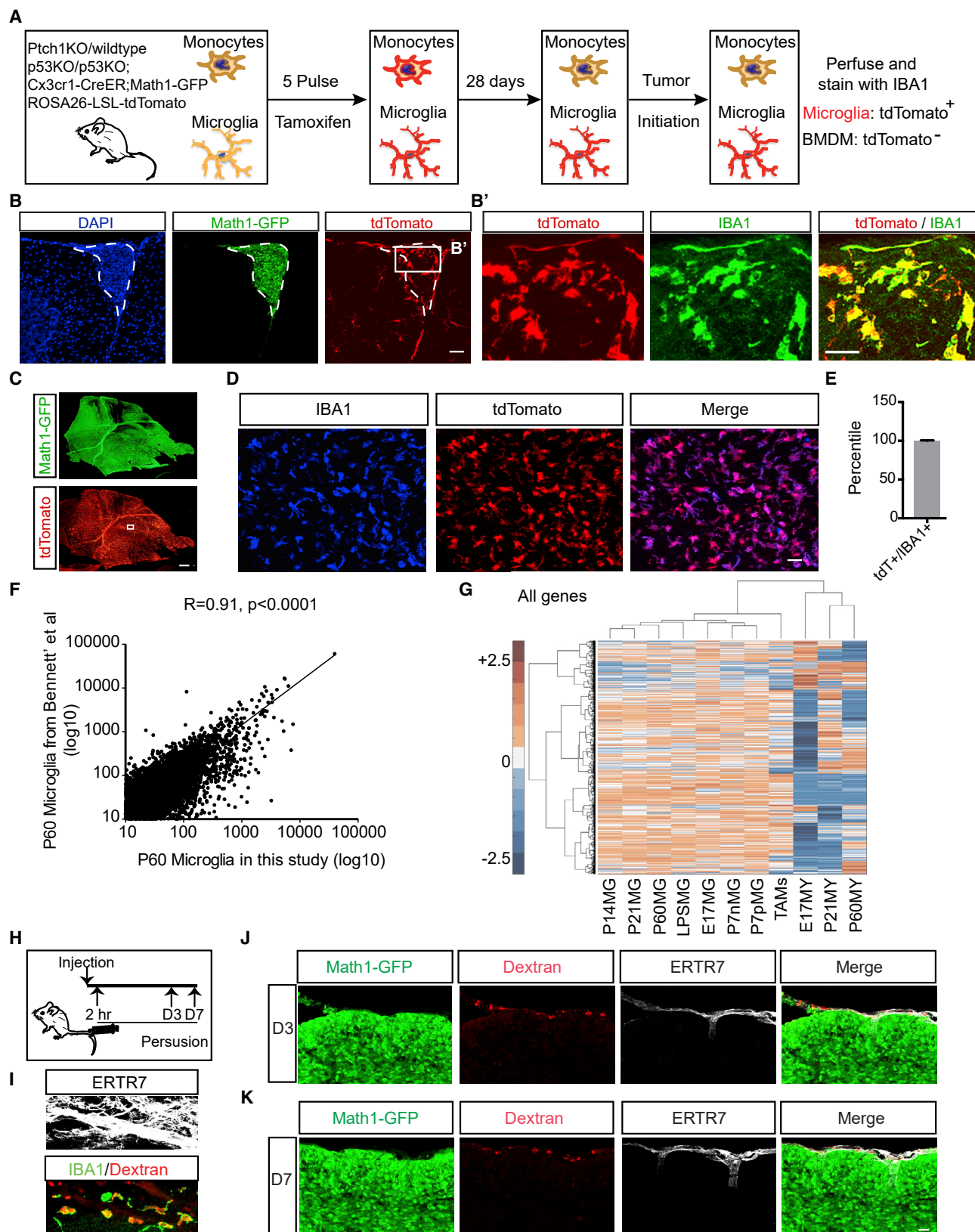
#### IL-4 Is Produced by TuAstrocytes

Finally, we set out to determine the cellular source of IL-4. Because it is known that Th2 lymphocytes are the major source of IL-4 (Bradding et al., 1992; Le Gros et al., 1990; Swain et al., 1990), we first comprehensively catalog the immune cell types in the TME after carefully removing immune cells in blood vessels with intracardiac perfusion with PBS. Our data indicated that more than 98% of CD45<sup>+</sup> immune cells in medulloblastoma were positive for the myeloid marker CD11b (Figure 7G). Considering the possibility of CD11b expression in activated T and B lymphocytes (Christensen et al., 2001; Ghosn et al., 2008; Kawai et al., 2005; Wagner et al., 2001) and mature natural killer (NK) cells (Omi et al., 2014), we performed further flow cytometry analysis for T cells (CD3), B cells (CD19), and NK cells (NK1.1). This analysis (Figure 7H), along with the lack of immunostaining of the T cell marker CD3 in the tumor mass (Figures S7E and S7F), indicated that only negligible numbers of T, B, and NK cells were present within the tumor mass. This finding corroborates well with reports in the literature that the predominant immune component in human medulloblastoma is CD11b<sup>+</sup> myeloid cells (Margol et al., 2015; Rossi et al., 1991). Taken together, the lack of infiltrated T cells led us to postulate that, rather than Th2 lymphocytes, other TME cells must be the source of IL-4.

We performed *in situ* analysis for IL-4 together with immunostaining for cell-type-specific markers to identify IL-4-producing cells. To our surprise, we identified GFAP<sup>+</sup> astrocytes as the major source of IL-4 (Figures 7I and 7J). To investigate whether IL-4 is produced by normal or tumor-derived astrocytes, we established a mouse model that incorporates both a tumor lineage marker (tdTomato) and an IL-4-GFP reporter transgene (Mohrs et al., 2001<sup>\*</sup> model B, illustrated in Figure S7G) and found that all IL-4-GFP<sup>+</sup> cells expressed both GFAP and tdTomato, suggesting that IL-4 is specifically produced by TuAstrocytes rather than normal astrocytes (Figures 7J and 7K; Figure S7H).

Scale bars are as follows: (A), 50  $\mu$ m; (B) and (E), 20  $\mu$ m; (I), 1 mm. Data are means  $\pm$  SD. One-way ANOVA (F and G) or Student's t test (C, D, and J); \* $p$  < 0.05, \*\* $p$  < 0.01, \*\*\* $p$  < 0.001.

See also Figure S5.



(legend on next page)

## DISCUSSION

Through comprehensive lineage tracing, molecular profiling, and functional studies, we demonstrated that TME components in ostensibly simple medulloblastoma form an intricate network to support tumor progression (Figure 7L). Our work clearly illustrates the importance of studying co-evolution of the TME and tumor cells at high spatiotemporal resolution using immunocompetent, injury-free genetic models and exemplifies how tumor plasticity contributes to cellular heterogeneity in the tumor mass and how multiple TME cells form a local community to promote tumor progression.

### The MADMs System Provides Temporospatial Resolution to Deconvolute the Complexity of the TME

The importance of TME for tumor progression has been well supported by a wealth of reports (Balkwill et al., 2012; Hanahan and Coussens, 2012; Quail and Joyce, 2013). Although tumor angiogenesis was the initial focus (Folkman, 1971), other TME cells, including fibroblasts, immune cells, and other tissue-resident cells, quickly took the stage (Binnewies et al., 2018; Gascard and Tlsty, 2016; Kalluri, 2016; Shiga et al., 2015; Tabuso et al., 2017). To develop novel cancer treatment strategies that target the TME, one must thoroughly study the establishment and functions of the TME with greater attention to time, space, cell lineage, as well as homotypic and heterotypic cell-cell interactions. Therefore, it is imperative to use high-resolution *in vivo* tools to delineate hierarchical organizations, reprogramming potentials, as well as clonal behaviors within the TME. The Confetti mouse is an example of such a tool that allows lineage tracing of multiple clones *in vivo*, which revealed not only the neutral competition mechanism of intestinal crypt homeostasis (Snippert et al., 2010) but also how cancer stem cells maintain tumor architecture to sustain intestinal adenomas (Schepers et al., 2012). On the other hand, the MADMs system is more suitable for dual-lineage analysis of the fate of one mutant and one WT cell from the same progenitor cell (Zong et al., 2005). Although previous applications of MADMs were focused on cell-autonomous gene functions in cancer (Gonzalez et al., 2018; Liu et al., 2011; Muzumdar et al., 2007), this study took advantage of its lineage-tracing capability to uncover tumor-TME relationships. The fact that such complexity of interactions could be unveiled from an ostensibly

“simple” cancer further emphasizes the importance of untangling the inner works of the TME in more complex tumors.

### *trans*-Differentiation of TuGNPs to TuAstrocytes: Community-Building Behaviors in the Tumor Mass

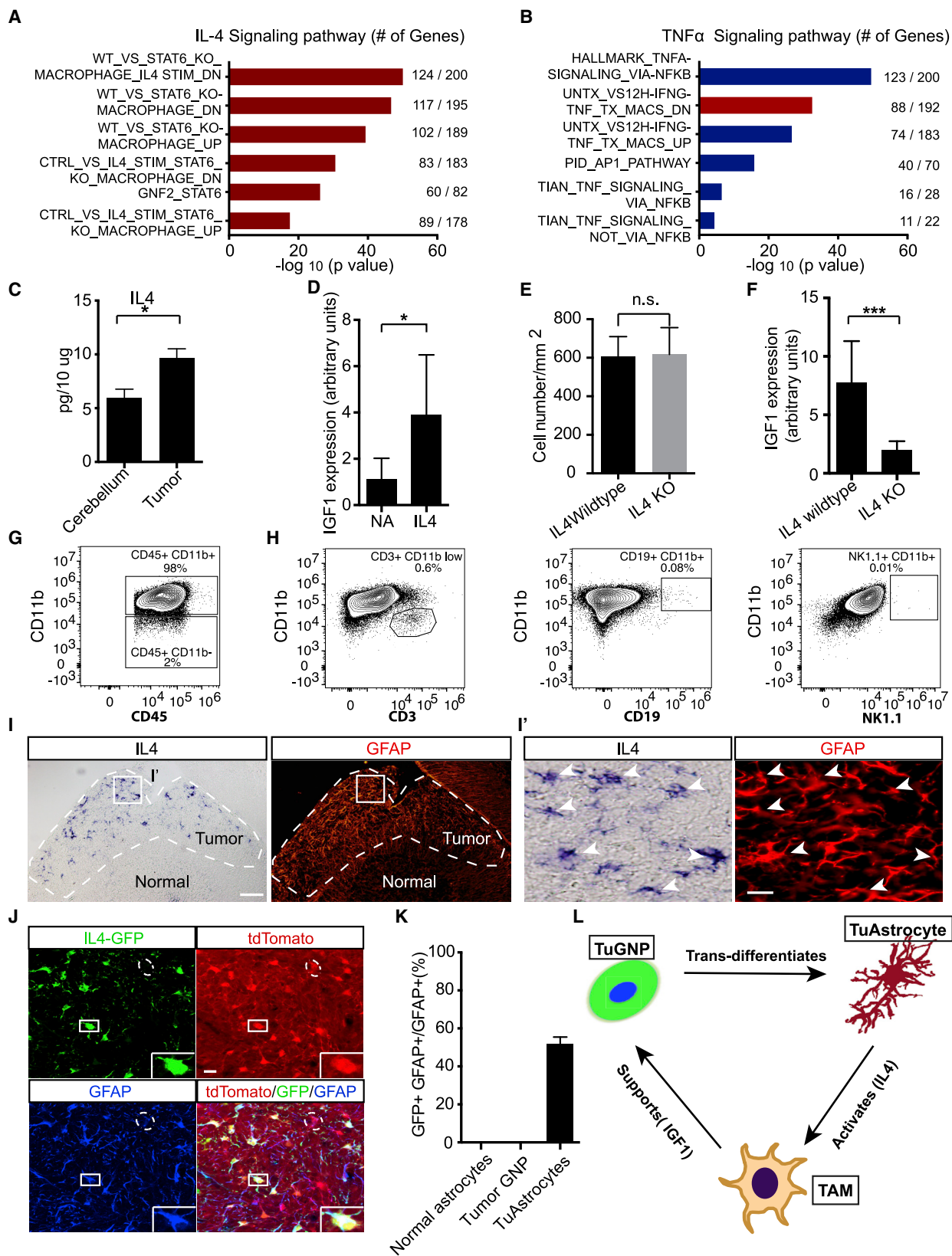
Relying on the lineage tracing capability of MADMs, we unexpectedly discovered the phenomenon of tumor-to-TME *trans*-differentiation. Fully aware of potential technical caveats, we painstakingly and exhaustively pursued all imaginable alternative explanations to exclude the possibility of cell fusion, protein transfer, ectopic Cre expression, and mis-expression of cell markers. Most importantly, karyotyping-based analysis of human medulloblastoma samples also demonstrated a lineage relationship between tumor GNPs and the astrocyte-like component in the tumor mass. The complementary nature between mouse genetics and human sample analysis greatly strengthens our confidence regarding this finding.

It should be noted that, although differentiation of tumor cells into other cell types has been reported before, the novelty of our findings lies within two aspects. First, *trans*-differentiation from GNPs to astrocytes has to overcome significant barriers within the developmental program because the GNP pool and astrocyte-producing neural stem cell pool are segregated temporally (from embryonic day 9.5 [E9.5] on during mouse embryonic development) and spatially (GNPs reside in the EGL on the surface of the cerebellar primordium, whereas neural stem cells (NSCs) reside in the ventricular zone, the innermost layer of the neural tube at the fourth ventricle). Second, although the functional contribution of *trans*-differentiated TuAstrocytes was unveiled in this study, it remains to be seen whether transdifferentiated cells in other tumor types also play such a significant functional role.

Still, there are many unanswered questions. First, what is the mechanism of *trans*-differentiation? Second, how is the ~1% composition of TuAstrocytes maintained throughout tumor progression? Finally, although we observed tantalizing hints of direct support of TuAstrocytes regarding tumor progression (Figures S3D–S3G), our study took an unexpected turn toward the discovery of the TuAstrocyte-TAM-tumor cell network. In the future, it will be important to investigate the direct supportive factors from TuAstrocytes toward tumor cells as well as to explore their role in blood-brain barrier (BBB) maintenance because

### Figure 6. TAMs Originate from Brain-Resident Microglia

(A) Schematic of the lineage tracing experiment.  
 (B and B') TdTomato<sup>+</sup> TAMs were present in small tumors (outlined with dotted lines, n = 3).  
 (C–E) TdTomato<sup>+</sup> TAMs overwhelmed the Math1-GFP<sup>+</sup> tumor mass in full-blown tumors; n = 5. Low magnification (C), high magnification (D), and quantification (E).  
 (F) Pearson correlation of transcriptomic data of P60 microglia between this study and a published dataset by Bennett et al. (2016) indicates that these two sets of data are highly correlated, allowing us to perform a hierarchical cluster analysis of the pooled data in (G).  
 (G) Hierarchical cluster analysis of transcriptomes showed that the gene expression profile of TAMs clusters with microglia rather than circulating myeloid cells. Abbreviations are as follows: P, postnatal; E, embryonic; numbers indicate embryonic or postnatal ages. MG, microglia; MY, circulating myeloid cells; P7nMG, TMEM119<sup>−</sup> microglia at P7; P7pMG, TMEM119<sup>+</sup> microglia at P7.  
 (H) Schematic illustration of dextran labeling of meningeal macrophages.  
 (I) The majority of meningeal macrophages were labeled by dextran via tail vein injection (75.79% + 7.77%, IBA1<sup>+</sup>dextran<sup>+</sup>/IBA1<sup>+</sup>).  
 (J and K) Macrophages within meninges (ERTR7<sup>+</sup>) did not infiltrate into the Math1-GFP<sup>+</sup> tumor mass 3 days (J) and 7 days (K) after dextran injection (n = 3). Scale bars are as follows: (B), (B'), and (D), 30 μm; (C), 200 μm; (J) and (K), 40 μm. n = 5 mice for each group. Data are means ± SD. Student's t test, \*\*\*\*p < 0.0001. See also Figure S6.



(legend on next page)

SHH-subtype medulloblastoma displayed little BBB disruption, in stark contrast to the Wnt-activated subtype (Phoenix et al., 2016).

### Harnessing the Uniqueness of the Neuro-immunological Network for Brain Tumor Treatment

Although our study discovered an anti-inflammatory immune network formed by TuAstrocytes and microglia in medulloblastoma, in other situations, microglia and astrocytes mutually activate each other to establish a pro-inflammatory environment (Liddel et al., 2017; Vainchtein et al., 2018). It is conceivable that one could re-polarize TuAstrocytes and TAMs if the proper conditions can be identified. Of course, such efforts must be grounded in the appreciation that microglia have a developmental origin distinct from macrophages (Ginhoux et al., 2010; Gomez Perdiguero et al., 2015) and tend to only mount subdued immune responses when aggravated (Bennett et al., 2016, 2018; Bennett et al., 2016; Gosselet et al., 2014, 2017) and that astrocytes are not “classical” immune cells and often play injury-repairing roles in the brain (Anderson et al., 2016; Burda and Sofroniew, 2014; Farina et al., 2007; Groves et al., 2018).

In addition to activating the innate immune system in the brain, attracting adaptive immune cells into the brain parenchyma, as found in neurological diseases, could facilitate brain tumor treatment (Baruch et al., 2013; Filiano et al., 2015; Hemmer et al., 2015). Although many checkpoint blockade-based immunotherapy clinical trials for brain tumors are currently underway (<https://clinicaltrials.gov>), limited success (Filley et al., 2017; Xue et al., 2017) emphasizes the need to carefully consider the unique immunological environment of the brain. Although infiltration of T cells has been reported previously in a glioma model (Quail et al., 2016), few T, B, or NK cells were found in our medulloblastoma model, which is in concordance with previous findings in human medulloblastoma samples (Margol et al., 2015; Rossi et al., 1991). Although this difference could be attributed either to different tumor types or to graft-induced injuries in the previous model, the possible absence of T cells nevertheless raises concern regarding the effectiveness of T cell-based immunotherapy for brain tumors. Even when T cells reach the tumor mass, critical cytokines for T cells, such as IL-2 and IL-15, were too low in our medulloblastoma model (Table S2) to support their survival. This finding corroborates well with recent clinical

research demonstrating that the presence of cytotoxic T cells had no correlation with overall survival of medulloblastoma patients (Vermeulen et al., 2017) and that T cell exhaustion is extremely severe in glioma (Woroniecka et al., 2018). Last but not least, one must take into consideration the fact that the brain is extremely sensitive to chemical and electrical imbalances and could be severely harmed by a cytokine storm or other overt immunological responses. Therefore, the efficacy of T cell-based immunotherapy in brain tumors will only manifest after we develop a firm grasp of neuro-immunology (Binnewies et al., 2018).

### Understanding the Intrinsic Stability of Tumors Based on Multilateral Paracrine Circuitry to Devise Effective Treatment Strategies

Although detailed molecular mechanisms warrant further exploration, our study clearly revealed an under-appreciated complexity of TME organization in medulloblastoma. Rather than one-on-one TME-tumor crosstalk, our data uncovered an intricate TME community in which *trans*-differentiation and a multilateral paracrine network support robust growth of tumor cells. It should be noted that, although signaling plasticity could partially explain the problem of therapeutic resistance in cancer, cellular plasticity and multi-cell networks could also contribute to tumor robustness. For example, an elegant modeling work demonstrated that a two-cell circuitry with reciprocally supportive paracrine factors could form a stable system to maintain tissue homeostasis that can withstand perturbations (Zhou et al., 2018). Conceivably, the three-cell system in medulloblastoma opens up even more channels of paracrine communication and would likely withstand severe perturbations during cancer therapy. Although this study was focused on the SHH subtype of medulloblastoma, it showcases a powerful technical platform that can be applied to deconstruct the TME network within other cancer types (Binnewies et al., 2018; Palucka and Coussens, 2016). The deepened understanding of TME-tumor cell relationships carries great promise for paradigm-shifting therapeutic strategies to cut off multiple paracrine crosstalks to fundamentally undermine the robustness of cancer.

### STAR★METHODS

Detailed methods are provided in the online version of this paper and include the following:

#### Figure 7. IL-4 Produced by TuAstrocytes Promotes IGF1 Expression in TAMs

(A and B) Pathway analysis of differentially expressed genes in TAMs revealed significantly upregulated signatures associated with IL-4 (A) but not TNF- $\alpha$  signaling (B).

(C) Luminex profiling showed that the IL-4 level was elevated in the tumor in comparison with normal cerebellum ( $n = 3$ ).

(D) IL-4 stimulation of acutely purified TAMs led to an elevated IGF1 level in culture ( $n = 5$ ).

(E) Quantification of the cell density of TAMs in IL-4 WT and IL-4 KO tumors.

(F) IL-4 KO led to a reduced IGF1 expression level in the tumor mass ( $n = 8$  for each genotype).

(G) Flow-cytometry analysis demonstrated that CD11b<sup>+</sup> myeloid cells were the dominant population of immune cells in the tumor ( $n = 10$ ).

(H) Negligible numbers of T, B, and NK cells were present ( $n = 4$ ).

(I and I') *In situ* hybridization showed that IL-4 was produced by GFAP<sup>+</sup> cells in the tumor mass.

(J) All IL4-GFP<sup>+</sup> cells were tdTomato<sup>+</sup> and GFAP<sup>+</sup>, suggesting that IL-4 was produced by TuAstrocytes ( $n = 3$ ).

(K) Quantitative analysis showed that IL-4 was expressed by ~50% TuAstrocytes but not by normal astrocytes or TuGNPs.

(L) Working model of an intricately organized TME network in medulloblastoma: a small fraction of tumor GNPs *trans*-differentiates into TuAstrocytes, which produce IL-4 to activate tumor-associated microglia (TAMs), which, in turn, secrete IGF1 to promote tumor progression.

Scale bars are as follows: (I), 50  $\mu$ m; (I') and (J), 20  $\mu$ m. Data are means  $\pm$  SD. Student's *t* test; \* $p < 0.05$ , \*\* $p < 0.01$ , \*\*\* $p < 0.001$ .

See also Figure S7 and Table S1.



- KEY RESOURCES TABLE
- LEAD CONTACT AND MATERIALS AVAILABILITY
- EXPERIMENTAL MODEL AND SUBJECT DETAILS
  - Mice
- METHOD DETAILS
  - Tamoxifen Administration
  - Tumor dissection and tumor weight measurement
  - Luminex
  - Quantitative PCR (qPCR)
  - Immunofluorescence staining and image processing
  - Quantification of TME cells throughout tumor development
  - RNA *In situ* hybridization
  - Fluorescent *In Situ* Hybridization of chromosome loci with immunofluorescence
  - Laser Capture Microdissection
  - RNA extraction, cDNA amplification, library construction and RNA sequencing of LCM micro-dissected tissues/cells
  - Primary tumor GNP purification and *in vitro* culture
  - Isolation of primary Tumor Associated Microglia/Macrophages (TAMs)
  - Co-culture of TAMs with Tumor GNPs
  - Flow cytometry
  - RNaseq and data analysis of TAMs
- QUANTIFICATION AND STATISTICAL ANALYSIS
- DATA AND CODE AVAILABILITY

## SUPPLEMENTAL INFORMATION

Supplemental Information can be found online at <https://doi.org/10.1016/j.cell.2019.12.024>.

## ACKNOWLEDGMENTS

We thank Tajie H. Harris, Chris Doe, David Rowitch, Praveen Raju, Melanie Rutkowski, and Jonathan Kipnis for critical discussions and insightful feedback; Ryan A. Llewellyn, Noel C. Derecki, James C. Cronk, and the UVA Flow Cytometry Core Facility for help with flow analysis; Fujun Qin for helping with GSEA; the UVA Advanced Microscopy Facility for imaging analysis; and Steffen Jung for providing the CX3CR1-CreER mouse line. This project was partially supported by grants DoD W81XWH-11-1-0557 and NIH R01NS097271 to H.Z., R01CA194470 and U01CA215794 to K.A.J., R21HL143025 to T.P.B., and R01NS055089 to C.G.E. P.B.V. was supported by NIH/NINDS pre-doctoral fellowship F31-NS076313. J.S.A.P. is supported by a Mark Foundation fellowship from the Cancer Research Institute, NCI 1K99CA237728-01, and the Burroughs Wellcome PDEP award. H.Z. and K.A.J. were Pew Scholars in Biomedical Sciences supported by the Pew Charitable Trusts.

## AUTHOR CONTRIBUTIONS

This work was designed by M.Y., P.B.V., Y.J., and H.Z. The main experiments were performed by M.Y., P.B.V., and Y.J. with assistance from Y.Y. and K.W. Human tumor materials and data were provided by F.J.R., C.G.E., L.Q., and X.-N.L. The laser capture microdissection experiment was performed by L.W. and M.Y. The sequencing analysis was performed by J.S.A.P., K.S.R., K.A.J., and C.C.G. The flow analysis was performed by R.B.C. and T.P.B. Microglia-specific antibodies were provided by M.L.B. and B.A.B. prior to publication. This manuscript was written by P.B.V., M.Y., Y.J., and H.Z. with input from all co-authors.

## DECLARATION OF INTERESTS

The authors declare no competing interests.

Received: June 7, 2019

Revised: October 16, 2019

Accepted: December 17, 2019

Published: January 23, 2020

## REFERENCES

- Abbott, N.J., Rönnbäck, L., and Hansson, E. (2006). Astrocyte-endothelial interactions at the blood-brain barrier. *Nat. Rev. Neurosci.* *7*, 41–53.
- Ahmed, F., and Haass, N.K. (2018). Microenvironment-Driven Dynamic Heterogeneity and Phenotypic Plasticity as a Mechanism of Melanoma Therapy Resistance. *Front. Oncol.* *8*, 173.
- Anders, S., and Huber, W. (2010). Differential expression analysis for sequence count data. *Genome Biol.* *11*, R106.
- Anderson, M.A., Burda, J.E., Ren, Y., Ao, Y., O’Shea, T.M., Kawaguchi, R., Coppola, G., Khakh, B.S., Deming, T.J., and Sofroniew, M.V. (2016). Astrocyte scar formation aids central nervous system axon regeneration. *Nature* *532*, 195–200.
- Arina, A., Idel, C., Hyjek, E.M., Alegre, M.L., Wang, Y., Bindokas, V.P., Weichselbaum, R.R., and Schreiber, H. (2016). Tumor-associated fibroblasts predominantly come from local and not circulating precursors. *Proc. Natl. Acad. Sci. USA* *113*, 7551–7556.
- Bailey, P., and Cushing, H. (1925). Medulloblastoma Cerebelli: a Common Type of Midcerebellar Glioma of Childhood. *Arch. Neurol. Psychiatry* *2*, 192.
- Balkwill, F.R., Capasso, M., and Hagemann, T. (2012). The tumor microenvironment at a glance. *J. Cell Sci.* *125*, 5591–5596.
- Baruch, K., Ron-Harel, N., Gal, H., Deczkowska, A., Shifrut, E., Ndfon, W., Miras-Neisberg, N., Cardon, M., Vaknin, I., Cahalon, L., et al. (2013). CNS-specific immunity at the choroid plexus shifts toward destructive Th2 inflammation in brain aging. *Proc. Natl. Acad. Sci. USA* *110*, 2264–2269.
- Bennett, M.L., Bennett, F.C., Liddel, S.A., Ajami, B., Zamanian, J.L., Fernhoff, N.B., Mulinyawe, S.B., Bohlen, C.J., Adil, A., Tucker, A., et al. (2016). New tools for studying microglia in the mouse and human CNS. *Proc. Natl. Acad. Sci. USA* *113*, E1738–E1746.
- Bennett, F.C., Bennett, M.L., Yaqoob, F., Mulinyawe, S.B., Grant, G.A., Hayden Gephart, M., Plowey, E.D., and Barres, B.A. (2018). A combination of ontogeny and CNS environment establishes microglial identity. *Neuron* *98*, 1170–1183.
- Binnewies, M., Roberts, E.W., Kersten, K., Chan, V., Fearon, D.F., Merad, M., Coussens, L.M., Gaborilovich, D.I., Ostrand-Rosenberg, S., Hedrick, C.C., et al. (2018). Understanding the tumor immune microenvironment (TIME) for effective therapy. *Nat. Med.* *24*, 541–550.
- Bradding, P., Feather, I.H., Howarth, P.H., Mueller, R., Roberts, J.A., Britten, K., Bews, J.P., Hunt, T.C., Okayama, Y., Heusser, C.H., et al. (1992). Interleukin 4 is localized to and released by human mast cells. *J. Exp. Med.* *176*, 1381–1386.
- Burda, J.E., and Sofroniew, M.V. (2014). Reactive gliosis and the multicellular response to CNS damage and disease. *Neuron* *81*, 229–248.
- Burger, P.C., Grahmann, F.C., Bliestle, A., and Kleihues, P. (1987). Differentiation in the medulloblastoma. A histological and immunohistochemical study. *Acta Neuropathol.* *73*, 115–123.
- Butovsky, O., Jedrychowski, M.P., Moore, C.S., Cialic, R., Lanser, A.J., Gabriely, G., Koeglsparger, T., Dake, B., Wu, P.M., Doykan, C.E., et al. (2014). Identification of a unique TGF- $\beta$ -dependent molecular and functional signature in microglia. *Nat. Neurosci.* *17*, 131–143.
- Chanmee, T., Ontong, P., Konno, K., and Itano, N. (2014). Tumor-associated macrophages as major players in the tumor microenvironment. *Cancers (Basel)* *6*, 1670–1690.

- Christensen, J.E., Andreasen, S.O., Christensen, J.P., and Thomsen, A.R. (2001). CD11b expression as a marker to distinguish between recently activated effector CD8(+) T cells and memory cells. *Int. Immunol.* *13*, 593–600.
- Chung, A.S., Lee, J., and Ferrara, N. (2010). Targeting the tumour vasculature: insights from physiological angiogenesis. *Nat. Rev. Cancer* *10*, 505–514.
- Colombo, E., and Farina, C. (2016). Astrocytes: Key Regulators of Neuroinflammation. *Trends Immunol.* *37*, 608–620.
- de Visser, K.E., Eichten, A., and Coussens, L.M. (2006). Paradoxical roles of the immune system during cancer development. *Nat. Rev. Cancer* *6*, 24–37.
- DeNardo, D.G., Barreto, J.B., Andreu, P., Vasquez, L., Tawfik, D., Kolhatkar, N., and Coussens, L.M. (2009). CD4(+) T cells regulate pulmonary metastasis of mammary carcinomas by enhancing protumor properties of macrophages. *Cancer Cell* *16*, 91–102.
- Deng, L., Zhou, J.F., Sellers, R.S., Li, J.F., Nguyen, A.V., Wang, Y., Orlofsky, A., Liu, Q., Hume, D.A., Pollard, J.W., et al. (2010). A novel mouse model of inflammatory bowel disease links mammalian target of rapamycin-dependent hyperproliferation of colonic epithelium to inflammation-associated tumorigenesis. *Am. J. Pathol.* *176*, 952–967.
- Dietrich, P., Dragatsis, I., Xuan, S., Zeitlin, S., and Efstratiadis, A. (2000). Conditional mutagenesis in mice with heat shock promoter-driven cre transgenes. *Mamm. Genome* *11*, 196–205.
- Dobin, A., Davis, C.A., Schlesinger, F., Drenkow, J., Zaleski, C., Jha, S., Batut, P., Chaisson, M., and Gingeras, T.R. (2013). STAR: ultrafast universal RNA-seq aligner. *Bioinformatics* *29*, 15–21.
- Doetsch, F., Caillé, I., Lim, D.A., García-Verdugo, J.M., and Alvarez-Buylla, A. (1999). Subventricular zone astrocytes are neural stem cells in the adult mammalian brain. *Cell* *97*, 703–716.
- Farina, C., Aloisi, F., and Meinl, E. (2007). Astrocytes are active players in cerebral innate immunity. *Trends Immunol.* *28*, 138–145.
- Filiano, A.J., Gadani, S.P., and Kipnis, J. (2015). Interactions of innate and adaptive immunity in brain development and function. *Brain Res.* *1617*, 18–27.
- Filley, A.C., Henriquez, M., and Dey, M. (2017). Recurrent glioma clinical trial, CheckMate-143: the game is not over yet. *Oncotarget* *8*, 91779–91794.
- Folkman, J. (1971). Tumor angiogenesis: therapeutic implications. *N. Engl. J. Med.* *285*, 1182–1186.
- Fournier, T., Riches, D.W., Winston, B.W., Rose, D.M., Young, S.K., Noble, P.W., Lake, F.R., and Henson, P.M. (1995). Divergence in macrophage insulin-like growth factor-I (IGF-I) synthesis induced by TNF-alpha and prostaglandin E2. *J. Immunol.* *155*, 2123–2133.
- Gabrilovich, D.I., Ostrand-Rosenberg, S., and Bronte, V. (2012). Coordinated regulation of myeloid cells by tumours. *Nat. Rev. Immunol.* *12*, 253–268.
- Gajewski, T.F., Schreiber, H., and Fu, Y.X. (2013). Innate and adaptive immune cells in the tumor microenvironment. *Nat. Immunol.* *14*, 1014–1022.
- Gascard, P., and Tlsty, T.D. (2016). Carcinoma-associated fibroblasts: orchestrating the composition of malignancy. *Genes Dev.* *30*, 1002–1019.
- Ghosn, E.E., Yang, Y., Tung, J., Herzenberg, L.A., and Herzenberg, L.A. (2008). CD11b expression distinguishes sequential stages of peritoneal B-1 development. *Proc. Natl. Acad. Sci. USA* *105*, 5195–5200.
- Gilbertson, R.J., and Ellison, D.W. (2008). The origins of medulloblastoma subtypes. *Annu. Rev. Pathol.* *3*, 341–365.
- Ginhoux, F., Greter, M., Leboeuf, M., Nandi, S., See, P., Gokhan, S., Mehler, M.F., Conway, S.J., Ng, L.G., Stanley, E.R., et al. (2010). Fate mapping analysis reveals that adult microglia derive from primitive macrophages. *Science* *330*, 841–845.
- Goldmann, T., Wieghofer, P., Müller, P.F., Wolf, Y., Varol, D., Yona, S., Brendecke, S.M., Kierdorf, K., Staszewski, O., Datta, M., et al. (2013). A new type of microglia gene targeting shows TAK1 to be pivotal in CNS autoimmune inflammation. *Nat. Neurosci.* *16*, 1618–1626.
- Goldmann, T., Wieghofer, P., Jordão, M.J., Prutek, F., Hagemeyer, N., Frenzel, K., Amann, L., Staszewski, O., Kierdorf, K., Krueger, M., et al. (2016). Origin, fate and dynamics of macrophages at central nervous system interfaces. *Nat. Immunol.* *17*, 797–805.
- Gomez Perdiguero, E., Klapproth, K., Schulz, C., Busch, K., Azzoni, E., Crozet, L., Garner, H., Trouillet, C., de Bruijn, M.F., Geissmann, F., and Rodewald, H.R. (2015). Tissue-resident macrophages originate from yolk-sac-derived erythromyeloid progenitors. *Nature* *518*, 547–551.
- Gong, S., Zheng, C., Doughty, M.L., Losos, K., Didkovsky, N., Schambra, U.B., Nowak, N.J., Joyner, A., Leblanc, G., Hatten, M.E., and Heintz, N. (2003). A gene expression atlas of the central nervous system based on bacterial artificial chromosomes. *Nature* *425*, 917–925.
- Gonzalez, P.P., Kim, J., Galvao, R.P., Cruickshanks, N., Abounader, R., and Zong, H. (2018). p53 and NF 1 loss plays distinct but complementary roles in glioma initiation and progression. *Glia* *66*, 999–1015.
- Goodrich, L.V., Milenković, L., Higgins, K.M., and Scott, M.P. (1997). Altered neural cell fates and medulloblastoma in mouse patched mutants. *Science* *277*, 1109–1113.
- Gosselin, D., Link, V.M., Romanoski, C.E., Fonseca, G.J., Eichenfield, D.Z., Spann, N.J., Stender, J.D., Chun, H.B., Garner, H., Geissmann, F., and Glass, C.K. (2014). Environment drives selection and function of enhancers controlling tissue-specific macrophage identities. *Cell* *159*, 1327–1340.
- Gosselin, D., Skola, D., Coufal, N.G., Holtman, I.R., Schlachetzki, J.C.M., Sajti, E., Jaeger, B.N., O'Connor, C., Fitzpatrick, C., Pasillas, M.P., et al. (2017). An environment-dependent transcriptional network specifies human microglia identity. *Science* *356*, eaal3222.
- Groves, A., Kihara, Y., Jonnalagadda, D., Rivera, R., Kennedy, G., Mayford, M., and Chun, J. (2018). A functionally defined *in vivo* astrocyte population identified by c-Fos activation in a mouse model of multiple sclerosis modulated by S1P signaling: immediate-early astrocytes (*ieAstrocytes*). *eNeuro* *5*, ENEURO.0239-18.2018.
- Hanahan, D., and Coussens, L.M. (2012). Accessories to the crime: functions of cells recruited to the tumor microenvironment. *Cancer Cell* *21*, 309–322.
- Harris, T.H., Banigan, E.J., Christian, D.A., Konradt, C., Tait Wojno, E.D., Norose, K., Wilson, E.H., John, B., Weninger, W., Luster, A.D., et al. (2012). Generalized Lévy walks and the role of chemokines in migration of effector CD8+ T cells. *Nature* *486*, 545–548.
- Heintz, N. (2004). Gene expression nervous system atlas (GENSAT). *Nat. Neurosci.* *7*, 483.
- Hemmer, B., Kerschensteiner, M., and Korn, T. (2015). Role of the innate and adaptive immune responses in the course of multiple sclerosis. *Lancet Neurol.* *14*, 406–419.
- Henner, A., Ventura, P.B., Jiang, Y., and Zong, H. (2013). MADM-ML, a mouse genetic mosaic system with increased clonal efficiency. *PLoS ONE* *8*, e77672.
- Högglund, R.A., and Maghazachi, A.A. (2014). Multiple sclerosis and the role of immune cells. *World J. Exp. Med.* *4*, 27–37.
- Iadecola, C., and Nedergaard, M. (2007). Glial regulation of the cerebral microvasculature. *Nat. Neurosci.* *10*, 1369–1376.
- Jacks, T., Remington, L., Williams, B.O., Schmitt, E.M., Halachmi, S., Bronson, R.T., and Weinberg, R.A. (1994). Tumor spectrum analysis in p53-mutant mice. *Curr. Biol.* *4*, 1–7.
- Janes, K.A., Wang, C.C., Holmberg, K.J., Cabral, K., and Brugge, J.S. (2010). Identifying single-cell molecular programs by stochastic profiling. *Nat. Methods* *7*, 311–317.
- Kalluri, R. (2016). The biology and function of fibroblasts in cancer. *Nat. Rev. Cancer* *16*, 582–598.
- Kawai, K., Tsuno, N.H., Matsushashi, M., Kitayama, J., Osada, T., Yamada, J., Tsuchiya, T., Yoneyama, S., Watanabe, T., Takahashi, K., and Nagawa, H. (2005). CD11b-mediated migratory property of peripheral blood B cells. *J. Allergy Clin. Immunol.* *116*, 192–197.
- Kühn, R., Rajewsky, K., and Müller, W. (1991). Generation and analysis of interleukin-4 deficient mice. *Science* *254*, 707–710.
- Kumar, M.P., Du, J., Lagoudas, G., Jiao, Y., Sawyer, A., Drummond, D.C., Lauffenburger, D.A., and Raue, A. (2018). Analysis of Single-Cell RNA-Seq Identifies Cell-Cell Communication Associated with Tumor Characteristics. *Cell Rep.* *25*, 1458–1468.e4.

- Kurihara, T., Warr, G., Loy, J., and Bravo, R. (1997). Defects in macrophage recruitment and host defense in mice lacking the CCR2 chemokine receptor. *J. Exp. Med.* *186*, 1757–1762.
- Lake, F.R., Noble, P.W., Henson, P.M., and Riches, D.W. (1994). Functional switching of macrophage responses to tumor necrosis factor- $\alpha$  (TNF  $\alpha$ ) by interferons. Implications for the pleiotropic activities of TNF  $\alpha$ . *J. Clin. Invest.* *93*, 1661–1669.
- Le Gros, G., Ben-Sasson, S.Z., Seder, R., Finkelman, F.D., and Paul, W.E. (1990). Generation of interleukin 4 (IL-4)-producing cells in vivo and in vitro: IL-2 and IL-4 are required for in vitro generation of IL-4-producing cells. *J. Exp. Med.* *172*, 921–929.
- Lee, H.Y., Greene, L.A., Mason, C.A., and Manzini, M.C. (2009). Isolation and culture of post-natal mouse cerebellar granule neuron progenitor cells and neurons. *J. Vis. Exp.* (23), 990.
- Liddel, S.A., Guttenplan, K.A., Clarke, L.E., Bennett, F.C., Bohlen, C.J., Schirmer, L., Bennett, M.L., Münch, A.E., Chung, W.S., Peterson, T.C., et al. (2017). Neurotoxic reactive astrocytes are induced by activated microglia. *Nature* *541*, 481–487.
- Liu, J.L., Grinberg, A., Westphal, H., Sauer, B., Accili, D., Karas, M., and LeRoith, D. (1998). Insulin-like growth factor-I affects perinatal lethality and post-natal development in a gene dosage-dependent manner: manipulation using the Cre/loxP system in transgenic mice. *Mol. Endocrinol.* *12*, 1452–1462.
- Liu, C., Sage, J.C., Miller, M.R., Verhaak, R.G., Hippenmeyer, S., Vogel, H., Foreman, O., Bronson, R.T., Nishiyama, A., Luo, L., and Zong, H. (2011). Mosaic analysis with double markers reveals tumor cell of origin in glioma. *Cell* *146*, 209–221.
- Love, M.I., Huber, W., and Anders, S. (2014). Moderated estimation of fold change and dispersion for RNA-seq data with DESeq2. *Genome Biol.* *15*, 550.
- Machold, R., and Fishell, G. (2005). Math1 is expressed in temporally discrete pools of cerebellar rhombic-lip neural progenitors. *Neuron* *48*, 17–24.
- Madisen, L., Zwingman, T.A., Sunkin, S.M., Oh, S.W., Zariwala, H.A., Gu, H., Ng, L.L., Palmiter, R.D., Hawrylycz, M.J., Jones, A.R., et al. (2010). A robust and high-throughput Cre reporting and characterization system for the whole mouse brain. *Nat. Neurosci.* *13*, 133–140.
- Mannaji, H., Takeshita, I., Fukui, M., Ohta, M., and Kitamura, K. (1981). Glial fibrillary acidic protein in medulloblastoma. *Acta Neuropathol.* *55*, 63–69.
- Margol, A.S., Robison, N.J., Gnanachandran, J., Hung, L.T., Kennedy, R.J., Vali, M., Dhall, G., Finlay, J.L., Erdreich-Epstein, A., Krieger, M.D., et al. (2015). Tumor-associated macrophages in SHH subgroup of medulloblastomas. *Clin. Cancer Res.* *21*, 1457–1465.
- Marino, S., Vooijs, M., van Der Gulden, H., Jonkers, J., and Berns, A. (2000). Induction of medulloblastomas in p53-null mutant mice by somatic inactivation of Rb in the external granular layer cells of the cerebellum. *Genes Dev.* *14*, 994–1004.
- Matei, V., Pauley, S., Kaing, S., Rowitch, D., Beisel, K.W., Morris, K., Feng, F., Jones, K., Lee, J., and Fritzsche, B. (2005). Smaller inner ear sensory epithelia in Neurog 1 null mice are related to earlier hair cell cycle exit. *Dev. Dyn.* *234*, 633–650.
- Miller, M.R., Robinson, K.J., Cleary, M.D., and Doe, C.Q. (2009). TU-tagging: cell type-specific RNA isolation from intact complex tissues. *Nat. Methods* *6*, 439–441.
- Mohrs, M., Shinkai, K., Mohrs, K., and Locksley, R.M. (2001). Analysis of type 2 immunity in vivo with a bicistronic IL-4 reporter. *Immunity* *15*, 303–311.
- Mullor, J.L., Sánchez, P., and Ruiz i Altaba, A. (2002). Pathways and consequences: Hedgehog signaling in human disease. *Trends Cell Biol.* *12*, 562–569.
- Muzumdar, M.D., Luo, L., and Zong, H. (2007). Modeling sporadic loss of heterozygosity in mice by using mosaic analysis with double markers (MADM). *Proc. Natl. Acad. Sci. USA* *104*, 4495–4500.
- Nikodemova, M., and Watters, J.J. (2012). Efficient isolation of live microglia with preserved phenotypes from adult mouse brain. *J. Neuroinflammation* *9*, 147.
- Noy, R., and Pollard, J.W. (2014). Tumor-associated macrophages: from mechanisms to therapy. *Immunity* *41*, 49–61.
- Oliver, T.G., Read, T.A., Kessler, J.D., Mehmeti, A., Wells, J.F., Huynh, T.T., Lin, S.M., and Wechsler-Reya, R.J. (2005). Loss of patched and disruption of granule cell development in a pre-neoplastic stage of medulloblastoma. *Development* *132*, 2425–2439.
- Omi, A., Enomoto, Y., Kuniwa, T., Miyata, N., and Miyajima, A. (2014). Mature resting Ly6C(high) natural killer cells can be reactivated by IL-15. *Eur. J. Immunol.* *44*, 2638–2647.
- Özdemir, B.C., Pentcheva-Hoang, T., Carstens, J.L., Zheng, X., Wu, C.C., Simpson, T.R., Laklai, H., Sugimoto, H., Kahlert, C., Novitskiy, S.V., et al. (2014). Depletion of carcinoma-associated fibroblasts and fibrosis induces immunosuppression and accelerates pancreas cancer with reduced survival. *Cancer Cell* *25*, 719–734.
- Palucka, A.K., and Coussens, L.M. (2016). The Basis of oncoimmunology. *Cell* *164*, 1233–1247.
- Patro, R., Mount, S.M., and Kingsford, C. (2014). Sailfish enables alignment-free isoform quantification from RNA-seq reads using lightweight algorithms. *Nat. Biotechnol.* *32*, 462–464.
- Phoenix, T.N., Patmore, D.M., Boop, S., Boulos, N., Jacus, M.O., Patel, Y.T., Rousset, M.F., Finkelstein, D., Goumnerova, L., Perreault, S., et al. (2016). Medulloblastoma Genotype Dictates Blood Brain Barrier Phenotype. *Cancer Cell* *29*, 508–522.
- Pietsch, T., Waha, A., Koch, A., Kraus, J., Albrecht, S., Tonn, J., Sörensen, N., Berthold, F., Henk, B., Schmandt, N., et al. (1997). Medulloblastomas of the desmoplastic variant carry mutations of the human homologue of Drosophila patched. *Cancer Res.* *57*, 2085–2088.
- Polyak, K., Haviv, I., and Campbell, I.G. (2009). Co-evolution of tumor cells and their microenvironment. *Trends Genet.* *25*, 30–38.
- Prinz, M., Erny, D., and Hagemeyer, N. (2017). Ontogeny and homeostasis of CNS myeloid cells. *Nat. Immunol.* *18*, 385–392.
- Quail, D.F., and Joyce, J.A. (2013). Microenvironmental regulation of tumor progression and metastasis. *Nat. Med.* *19*, 1423–1437.
- Quail, D.F., Bowman, R.L., Akkari, L., Quick, M.L., Schuhmacher, A.J., Huse, J.T., Holland, E.C., Sutton, J.C., and Joyce, J.A. (2016). The tumor microenvironment underlies acquired resistance to CSF-1R inhibition in gliomas. *Science* *352*, aad3018.
- R Core Team, 2019. In: R: A language and environment for statistical computing. R Foundation for Statistical Computing, Vienna, Austria. <https://www.R-project.org/>.
- Ranke, M.B. (2015). Insulin-like growth factor binding-protein-3 (IGFBP-3). *Best Pract. Res. Clin. Endocrinol. Metab.* *29*, 701–711.
- Rickett, C.H., and Paulus, W. (2005). Prognosis-related histomorphological and immunohistochemical markers in central nervous system tumors of childhood and adolescence. *Acta Neuropathol.* *109*, 69–92.
- Rose, M.F., Ren, J., Ahmad, K.A., Chao, H.T., Klisch, T.J., Flora, A., Greer, J.J., and Zoghbi, H.Y. (2009). Math1 is essential for the development of hindbrain neurons critical for perinatal breathing. *Neuron* *64*, 341–354.
- Rossi, M.L., Buller, J.R., Heath, S.A., Carey, M.P., Carboni, P., Jr., Koutsoubelis, G., and Coakham, H.B. (1991). The monocyte/macrophage infiltrate in 35 medulloblastomas: a paraffin-wax study. *Tumori* *77*, 36–40.
- Schepers, A.G., Snippert, H.J., Stange, D.E., van den Born, M., van Es, J.H., van de Wetering, M., and Clevers, H. (2012). Lineage tracing reveals Lgr5+ stem cell activity in mouse intestinal adenomas. *Science* *337*, 730–735.
- Schofield, D., West, D.C., Anthony, D.C., Marshal, R., and Sklar, J. (1995). Correlation of loss of heterozygosity at chromosome 9q with histological subtype in medulloblastomas. *Am. J. Pathol.* *146*, 472–480.
- Schüller, U., Heine, V.M., Mao, J., Kho, A.T., Dillon, A.K., Han, Y.G., Huillard, E., Sun, T., Ligon, A.H., Qian, Y., et al. (2008). Acquisition of granule neuron precursor identity is a critical determinant of progenitor cell competence to form Shh-induced medulloblastoma. *Cancer Cell* *14*, 123–134.

- Shee, K., Yang, W., Hinds, J.W., Hampsch, R.A., Varn, F.S., Traphagen, N.A., Patel, K., Cheng, C., Jenkins, N.P., Kettenbach, A.N., et al. (2018). Therapeutically targeting tumor microenvironment-mediated drug resistance in estrogen receptor-positive breast cancer. *J. Exp. Med.* *215*, 895–910.
- Shiga, K., Hara, M., Nagasaki, T., Sato, T., Takahashi, H., and Takeyama, H. (2015). Cancer-Associated Fibroblasts: Their Characteristics and Their Roles in Tumor Growth. *Cancers (Basel)* *7*, 2443–2458.
- Shu, Q., Wong, K.K., Su, J.M., Adesina, A.M., Yu, L.T., Tsang, Y.T., Antalfy, B.C., Baxter, P., Perlaky, L., Yang, J., et al. (2008). Direct orthotopic transplantation of fresh surgical specimen preserves CD133+ tumor cells in clinically relevant mouse models of medulloblastoma and glioma. *Stem Cells* *26*, 1414–1424.
- Siebert, H., Sachse, A., Kuziel, W.A., Maeda, N., and Brück, W. (2000). The chemokine receptor CCR2 is involved in macrophage recruitment to the injured peripheral nervous system. *J. Neuroimmunol.* *110*, 177–185.
- Singh, S., Wang, L., Schaff, D.L., Sutcliffe, M.D., Koeppl, A.F., Kim, J., Onengut-Gumuscu, S., Park, K.S., Zong, H., and Janes, K.A. (2019). In situ 10-cell RNA sequencing in tissue and tumor biopsy samples. *Sci. Rep.* *9*, 4836.
- Snippert, H.J., van der Flier, L.G., Sato, T., van Es, J.H., van den Born, M., Kroon-Veenboer, C., Barker, N., Klein, A.M., van Rheenen, J., Simons, B.D., and Clevers, H. (2010). Intestinal crypt homeostasis results from neutral competition between symmetrically dividing Lgr5 stem cells. *Cell* *143*, 134–144.
- Soneson, C., Love, M.I., and Robinson, M.D. (2015). Differential analyses for RNA-seq: transcript-level estimates improve gene-level inferences. *F1000Res.* *4*, 1521.
- Spadaro, O., Camell, C.D., Bosurgi, L., Nguyen, K.Y., Youm, Y.H., Rothlin, C.V., and Dixit, V.D. (2017). IGF1 Shapes Macrophage Activation in Response to Immunometabolic Challenge. *Cell Rep.* *19*, 225–234.
- Stockmann, C., Schadendorf, D., Klose, R., and Helfrich, I. (2014). The impact of the immune system on tumor: angiogenesis and vascular remodeling. *Front. Oncol.* *4*, 69.
- Straussman, R., Morikawa, T., Shee, K., Barzily-Rokni, M., Qian, Z.R., Du, J., Davis, A., Mongare, M.M., Gould, J., Frederick, D.T., et al. (2012). Tumour micro-environment elicits innate resistance to RAF inhibitors through HGF secretion. *Nature* *487*, 500–504.
- Su, S., Chen, J., Yao, H., Liu, J., Yu, S., Lao, L., Wang, M., Luo, M., Xing, Y., Chen, F., et al. (2018). CD10+GPR77+ cancer-associated fibroblasts promote cancer formation and chemoresistance by sustaining cancer stemness. *Cell* *172*, 841–856.
- Sun, Y. (2016). Tumor microenvironment and cancer therapy resistance. *Cancer Lett.* *380*, 205–215.
- Swain, S.L., Weinberg, A.D., English, M., and Huston, G. (1990). IL-4 directs the development of Th2-like helper effectors. *J. Immunol.* *145*, 3796–3806.
- Tabori, U., Baskin, B., Shago, M., Alon, N., Taylor, M.D., Ray, P.N., Bouffet, E., Malkin, D., and Hawkins, C. (2010). Universal poor survival in children with medulloblastoma harboring somatic TP53 mutations. *J. Clin. Oncol.* *28*, 1345–1350.
- Tabuso, M., Homer-Vanniasinkam, S., Adya, R., and Arasaradnam, R.P. (2017). Role of tissue microenvironment resident adipocytes in colon cancer. *World J. Gastroenterol.* *23*, 5829–5835.
- Vainchtein, I.D., Chin, G., Cho, F.S., Kelley, K.W., Miller, J.G., Chien, E.C., Lidell, S.A., Nguyen, P.T., Nakao-Inoue, H., Dorman, L.C., et al. (2018). Astrocyte-derived interleukin-33 promotes microglial synapse engulfment and neural circuit development. *Science* *359*, 1269–1273.
- Vermeulen, J.F., Van Hecke, W., Adriaansen, E.J.M., Jansen, M.K., Bouma, R.G., Villacorta Hidalgo, J., Fisch, P., Broekhuizen, R., Spliet, W.G.M., Kool, M., and Bovenschen, N. (2017). Prognostic relevance of tumor-infiltrating lymphocytes and immune checkpoints in pediatric medulloblastoma. *Oncotology* *7*, e1398877.
- Wagner, C., Hänsch, G.M., Stegmaier, S., Deneff, B., Hug, F., and Schoels, M. (2001). The complement receptor 3, CR3 (CD11b/CD18), on T lymphocytes: activation-dependent up-regulation and regulatory function. *Eur. J. Immunol.* *31*, 1173–1180.
- Wang, L., and Janes, K.A. (2013). Stochastic profiling of transcriptional regulatory heterogeneities in tissues, tumors and cultured cells. *Nat. Protoc.* *8*, 282–301.
- Weinberg, R.A. (2008). Coevolution in the tumor microenvironment. *Nat. Genet.* *40*, 494–495.
- Wetmore, C., Eberhart, D.E., and Curran, T. (2001). Loss of p53 but not ARF accelerates medulloblastoma in mice heterozygous for patched. *Cancer Res.* *61*, 513–516.
- Wojtowicz, J.M., and Kee, N. (2006). BrdU assay for neurogenesis in rodents. *Nat. Protoc.* *1*, 1399–1405.
- Woroniecka, K., Chongsathidkiet, P., Rhodin, K., Kemeny, H., Dechant, C., Farber, S.H., Elsamadicy, A.A., Cui, X., Koyama, S., Jackson, C., et al. (2018). T-Cell Exhaustion Signatures Vary with Tumor Type and Are Severe in Glioblastoma. *Clin. Cancer Res.* *24*, 4175–4186.
- Wright, J.H. (1910). Neurocytoma or Neuroblastoma, a Kind of Tumor Not Generally Recognized. *J. Exp. Med.* *12*, 556–561.
- Wyckoff, J., Wang, W., Lin, E.Y., Wang, Y., Pixley, F., Stanley, E.R., Graf, T., Pollard, J.W., Segall, J., and Condeelis, J. (2004). A paracrine loop between tumor cells and macrophages is required for tumor cell migration in mammary tumors. *Cancer Res.* *64*, 7022–7029.
- Wynes, M.W., and Riches, D.W. (2003). Induction of macrophage insulin-like growth factor-I expression by the Th2 cytokines IL-4 and IL-13. *J. Immunol.* *171*, 3550–3559.
- Xue, S., Hu, M., Iyer, V., and Yu, J. (2017). Blocking the PD-1/PD-L1 pathway in glioma: a potential new treatment strategy. *J. Hematol. Oncol.* *10*, 81.
- Yang, Z.J., Ellis, T., Markant, S.L., Read, T.A., Kessler, J.D., Bourbonlous, M., Schüller, U., Machold, R., Fishell, G., Rowitch, D.H., et al. (2008). Medulloblastoma can be initiated by deletion of Patched in lineage-restricted progenitors or stem cells. *Cancer Cell* *14*, 135–145.
- Yona, S., Kim, K.W., Wolf, Y., Mildner, A., Varol, D., Breker, M., Strauss-Ayali, D., Viukov, S., Guillems, M., Misharin, A., et al. (2013). Fate mapping reveals origins and dynamics of monocytes and tissue macrophages under homeostasis. *Immunity* *38*, 79–91.
- Zhang, L., and Goldman, J.E. (1996). Developmental fates and migratory pathways of dividing progenitors in the postnatal rat cerebellum. *J. Comp. Neurol.* *370*, 536–550.
- Zhao, C.T., Li, K., Li, J.T., Zheng, W., Liang, X.J., Geng, A.Q., Li, N., and Yuan, X.B. (2009). PKCdelta regulates cortical radial migration by stabilizing the Cdk5 activator p35. *Proc. Natl. Acad. Sci. USA* *106*, 21353–21358.
- Zhao, X., Liu, Z., Yu, L., Zhang, Y., Baxter, P., Voicu, H., Gurusiddappa, S., Luan, J., Su, J.M., Leung, H.C., and Li, X.N. (2012). Global gene expression profiling confirms the molecular fidelity of primary tumor-based orthotopic xenograft mouse models of medulloblastoma. *Neuro-oncol.* *14*, 574–583.
- Zhou, X., Franklin, R.A., Adler, M., Jacox, J.B., Bailis, W., Shyer, J.A., Flavell, R.A., Mayo, A., Alon, U., and Medzhitov, R. (2018). Circuit design features of a stable two-cell system. *Cell* *172*, 744–757.
- Zong, H., Espinosa, J.S., Su, H.H., Muzumdar, M.D., and Luo, L. (2005). Mosaic analysis with double markers in mice. *Cell* *121*, 479–492.

## STAR★METHODS

## KEY RESOURCES TABLE

REAGENT or RESOURCE	SOURCE	IDENTIFIER
Antibodies		
rabbit anti-GFAP antibody	Dako	Cat#Z0334; RRID: AB_10013382
rabbit anti-GFAP antibody	Abcam	Cat#ab7260; RRID: AB_30580
rabbit anti-BLBP antibody	Millipore	Cat#AB9558; RRID: AB_2314014
chicken anti-GFP antibody	Aves Labs	Cat#GFP-1020; RRID: AB_10000240
goat anti-c-Myc Antibody	Novus Biochemicals	Cat#NB600-338; RRID: AB_10001879
rat anti-BrdU antibody	Accurate Chemical & Scientific Corporation	Cat#OBT0030; RRID: AB_2313756
sheep Anti-Digoxigenin Fab fragments Antibody, AP Conjugated	Roche	Cat#11093274910; RRID: AB_514497
Armenian Hamster anti-CD3	eBioscience	Cat#14-0031-82; RRID: AB_467049
rabbit anti-NeuN	Abcam	Cat#ab177487; RRID: AB_2532109
rabbit anti-P2ry12	AnaSpec	Cat#55043A; RRID: AB_2298886
rabbit anti-ER-TR7	Abcam	Cat#ab51824; RRID: AB_881651
goat anti-PDGFRalpha	R&D	Cat#AF1062; RRID: AB_2236897
rabbit anti-TMEM119	Abcam	Cat#ab185333; RRID: AB_2687894
rabbit anti-Iba 1	Wako	Cat#019-19741; RRID: AB_839504
rabbit anti-cleaved caspase 3	Cell Signaling Technology	Cat#9661; RRID: AB_2341188
rabbit anti-CD31	Thermo Fisher Scientific	Cat#MA5-16337; RRID: AB_2537856
mouse anti-hNA	millipore	Cat#MAB1281; RRID: AB_94090
mouse anti-hGFAP	Covance	Cat#SMI-21R-100; RRID: AB_509978
mouse anti-Ki67	BD Biosciences	Cat#556003; RRID: AB_396287
rabbit anti-CD68	Bio-Rad	Cat#MCA1957GA; RRID: AB_324217
Alexa Flour 647-CD192(CCR2)	eBioscience	Cat#150612; RRID: AB_2616984
Anti-mouse CD16/32	eBioscience	Cat#14-0161-82; RRID: AB_467133
PE/Cy7-CD45	BioLegend	Cat#103223; RRID: AB_313006
BV421-CD11b	BD Bioscience	Cat#562605; RRID: AB_11152949
PE-CD3	eBioscience	Cat#14-0031-82; RRID: AB_467049
PE/Cy7-CD19	eBioscience	Cat#25-0193-82; clone1D3; RRID: AB_925735)
APC-CD45	BD Bioscience	Cat#559864 clone 30-F11; RRID: AB_398672)
Biotin-NK1.1	BioLegend	Cat#108703, clone PK136; RRID: AB_313390
SA-BV605	BD Bioscience	Cat#563260; RRID: AB_2738383
R-phycoerythrin goat anti-rabbit IgG	Life Technologies	Cat#P2771MP
Alexa 488 Donkey Anti-Mouse IgG (H+L)	Thermo Fisher Scientific	Cat#A21202; RRID: Ab_141607
Alexa-555 Donkey Anti-Mouse IgG (H+L)	Thermo Fisher Scientific	Cat#A31570; RRID: B_2536180
Alexa-647 Donkey Anti-Mouse IgG (H+L)	Thermo Fisher Scientific	Cat#A31571; RRID: AB_162542
Alexa 488 Donkey Anti-Rabbit IgG (H+L)	Thermo Fisher Scientific	Cat#711-545-152; RRID: AB_2313584
Alexa-555 Donkey Anti-Rabbit IgG (H+L)	Thermo Fisher Scientific	Cat#A31572; RRID: AB_162543
Alexa-647 Donkey Anti- Rabbit IgG (H+L)	Thermo Fisher Scientific	Cat#711-605-152; RRID: AB_2492288
Alexa-555 Donkey Anti-Rat IgG (H+L)	Thermo Fisher Scientific	Cat#712-165-150; RRID: AB_2340666
Alexa-647 Donkey Anti- Armenian Hamster IgG (H+L)	Thermo Fisher Scientific	Cat#127-495-160; RRID: AB_2338995
Alexa-647 Donkey Anti-Rat IgG (H+L)	Jackson Immuno Research Labs	Cat#712-605-153; RRID: AB_2340694

(Continued on next page)

**Continued**

REAGENT or RESOURCE	SOURCE	IDENTIFIER
<b>Bacterial and Virus Strains</b>		
NEB® 5-alpha Competent <i>E. coli</i> (High Efficiency)	NEB	C2987
<b>Biological Samples</b>		
Mouse tumor, cortex, spinal cord	This study	N/A
Human medulloblastoma	John Hopkins Hospital pathology core	N/A
<b>Chemicals</b>		
Dextran – 10 KD, Tetramethylrhodamine	Thermo Fisher Scientific	D1817
Tamoxifen	Sigma	T5648
Tamoxifen tablet	Actavis	NDC 0591-2473-30
sunflower oil	Sigma	S5007
MinElute PCR Purification Kit	QIAGEN	ID: 28004
iScript cDNA Synthesis Kit, 100 × 20 µl rxns	Bio-Rad	Cat#1708891
AMPure XP bead	Bechman	REF A63881
Qubit assay	Life Technology	REF Q32850
SuperScript III	Invitrogen	18080-044
RNAqueous-Micro kit	Ambion	AM1931
LCM caps	Applied Biosystems	LCM0214
Proteinase K	Sigma	P2308
RNase H	Amersham	E70054Z
5x terminal transferase buffer	Invitrogen	16314-015
dNTP	Roche	11277049001
High Fidelity PCR system	Roche	11732650001
PMSF	Sigma	P7626
Terminal transferase	Roche	3333575001
10x ThermoPol buffer	New England Biolabs	B9005S
AmpliTaq polymerase	Applied Biosystems	N8080156
0.5ml thin-walled PCR tube	Applied Biosystems	N8010611
0.2ml thin-walled PCR tube	Applied Biosystems	N8010612
SP6 RNA polymerase	Roche	Cat#11 487 671 001
T7 RNA polymerase	Roche	Cat#11 881 775 001
Protector RNase Inhibitor	Roche	Cat#03 335 399 001
BCIP®/NBT Alkaline Phosphatase Substrate	Roche	B5655
DNase I recombinant	Roche	Cat#04 716 728 001
TRIzol reagent	ThermoFisher Scientific	Cat#5596018
pGEM®-T Easy Vector Systems	Promega	A1360
<b>Peptides and Recombinant Proteins</b>		
Mouse IL4	R&D	Cat#404-ML/CF
Insulin from bovine pancreas	Sigma-Aldrich	I6634
Human HGF	Peptotech	Cat#100-39
Mouse HGF	Peptotech	Cat#315-23
Mouse IGF1	Peptotech	Cat#250-19
Human IGF1	Peptotech	Cat#100-11
IGFBP3	Sigma	Cat#SRP3067-25UG
<b>Critical Commercial Assays</b>		
CD11b MACS beads	Miltenyi Biotec	Cat#130-093-634
Luminex Panel	Millipore	Cat#MCYTOMAG-70K

(Continued on next page)

<b>Continued</b>		
REAGENT or RESOURCE	SOURCE	IDENTIFIER
EdU Click assay	Invitrogen	Cat#A10277
DIG RNA Labeling Mix	Roche	Cat#11 277 073 910
Deposited Data		
LCM Tumor Astrocyte RNaseq	This paper	GEO: GSE111734
Tumor associate microglia RNaseq	This paper	GEO: GSE109750
microglia RNaseq	<a href="#">Bennett et al., 2016</a>	NCBI BioProject: PRJNA307271
Experimental Models: Cell Lines		
Tumor cell primary culture	This study	N/A
Tumor Associate microglia primary culture	This study	N/A
Tumor sphere primary culture	This study	N/A
Human Medulloblastoma Cell	<a href="#">Shu et al., 2008</a>	N/A
Experimental Models: Organisms/Strains		
TG11ML, GT11ML	<a href="#">Henner et al., 2013</a>	JAX#030578
IGF1Rflox/flox	<a href="#">Dietrich et al., 2000</a>	JAX#012251
IGF1flox/flox	<a href="#">Liu et al., 1998</a>	JAX#016831
CSF1R-iCre	<a href="#">Deng et al., 2010</a>	JAX#021024
CX3CR1-CreER <sup>T2</sup>	<a href="#">Yona et al., 2013</a>	N/A
Ptch1-KO	<a href="#">Goodrich et al., 1997</a>	JAX#003081
p53-KO	<a href="#">Jacks et al., 1994</a>	JAX#002101
p53-flox	<a href="#">Marino et al., 2000</a>	JAX#008462
Math1-Cre	<a href="#">Matei et al., 2005</a>	JAX#011104
Math1-CreER <sup>T2</sup>	<a href="#">Machold and Fishell, 2005</a>	JAX#007684
Math1-GFP	<a href="#">Rose et al., 2009</a>	JAX#013593
IL4-GFP reporter	<a href="#">Mohrs et al., 2001</a>	JAX#004190
IL4-KO	<a href="#">Kühn et al., 1991</a>	JAX#002253
Rosa26-LSL-tdTomato	<a href="#">Madisen et al., 2010</a>	JAX#007908
Aldh1l1-GFP	<a href="#">Heintz, 2004</a>	GENESAT (MMRRC#011015-UCD)
Oligonucleotides		
See <a href="#">Table S3</a>	This study	N/A
Software and Algorithms		
GSEA	Broad Institute	<a href="https://www.broadinstitute.org/gsea/index.jsp">https://www.broadinstitute.org/gsea/index.jsp</a>
GraphPad Prism 6.00	GraphPad	<a href="https://www.graphpad.com/">https://www.graphpad.com/</a>
R language	<a href="#">R Core Team, 2019</a> The R Project for Statistical Computing	<a href="http://www.r-project.org">http://www.r-project.org</a>
MATLAB	The MathWorks	<a href="https://www.mathworks.com/products/matlab.html">https://www.mathworks.com/products/matlab.html</a>

## LEAD CONTACT AND MATERIALS AVAILABILITY

All Plasmid, Cell lines, tumor mouse model generated in this study will be made available upon request to the Lead Contact. Further information and requests for resources may be directed to, and will be fulfilled by the Lead Contact, Hui Zong ([hz9s@virginia.edu](mailto:hz9s@virginia.edu)).

## EXPERIMENTAL MODEL AND SUBJECT DETAILS

### Mice

C57BL6 was obtained from Charles River. MADM-ML pair TG11ML, GT11ML JAX# 030578 ([Henner et al., 2013](#)), IGF1R-flox ([Dietrich et al., 2000](#)), IGF1-flox ([Liu et al., 1998](#)), CSF1R-iCre ([Deng et al., 2010](#)), CX3CR1-CreERT2 ([Yona et al., 2013](#)), Ptch1-KO JAX#

003081 (Goodrich et al., 1997), p53-KO JAX# 002101 (Jacks et al., 1994), p53-flox JAX# 008462 (Marino et al., 2000), Math1-Cre JAX# 011104 (Matei et al., 2005), Math1-CreER<sup>T2</sup> (Machold and Fishell, 2005), Math1-GFP JAX# 013593 (Rose et al., 2009), IL4-GFP reporter (Mohrs et al., 2001), IL4-KO (Kühn et al., 1991), and Rosa26-LSL-tdTomato JAX# 007908 (Madisen et al., 2010) were obtained from Jackson Laboratory or colleagues. Aldh1L1-GFP was ordered from Genesat (MMRRC# 011015-UCD) (Heintz, 2004). For all *in vivo* experiments, the ages of mice were indicated in figures or figure legends. Mice were separated into experimental groups on the basis of genotype and age. Female and male mice were used for all experiments to exclude gender effects. All animal procedures, including housing conditions and husbandry routines were performed according to the protocols approved by the Institutional Animal Care and Use Committee (IACUC) of the University of Virginia. Statistical tests were used to predetermine sample size of tumor mice. All mice are healthy, immune-competent except for genetic mutations introduced for experimental purposes. Prior to experiments, they were not involved in previous procedures and remained drug- and test-naive.

To test distinct hypotheses, in total we used ~10 mouse models in this study, which were derived from 4 basic models depicted in Table S1.

## METHOD DETAILS

### Tamoxifen Administration

For adult mice, tamoxifen citrate tablets (20 mg/tablet; Mylan) were ground and dissolved in saline at 20 mg/ml and delivered via oral gavage.

### Tumor dissection and tumor weight measurement

To obtain the tumor weight, tumor-bearing mice were sacrificed at corresponding age. Tumor tissues (GFP+) was carefully dissected out under fluorescence microscopy and weighed by analytical balances.

### Luminex

Tumor or normal cerebellum tissues were dissected out and flash-frozen in liquid nitrogen. Frozen tissue pieces were then ground up and lysed in Tissue Extraction Reagent I (Life Technologies) supplemented with protease inhibitors and phosphatase inhibitors. The protein concentration of the lysate was determined by Pierce<sup>TM</sup> BCA protein Assay Kit (Thermo Scientific). All samples were adjusted to 1mg/ml with Tissue Extraction Reagent I and submitted to UVA Flow Cytometry Core Facility to run a 32-plex cytokine/chemokine/growth factor panel on Luminex MAGPIX system. This 32-plex panel includes IL-1, IL-2, IL-3, IL-4, IL-5, IL-6, IL-7, IL-9, IL-10, IL-12, IL-13, IL-15, IL-17, Eotaxin, CXCL-10, KC/GRO, MCP-1, MIP-1, MIP-2, MIG, LIF, Rantes, LIX, IFN, TNF, GM-CSF, M-CSF, G-CSF and VEGF. 25 µg total proteins extracted from tumor tissue and adjacent normal cerebellum were used for Luminex analysis. The concentration of each cytokine/chemokine/growth factor was normalized to total protein amount.

### Quantitative PCR (qPCR)

We performed real-time PCR as described previously (Liu et al., 2011). Briefly, Total RNA was isolated from cells/tissues using TRIzol reagent (Invitrogen) followed by phenol/chloroform extraction and ethanol precipitation according to the method previously described (Miller et al., 2009). To extract total RNA from small quantity of cells/tissues or to obtain high quality RNA, RNeasy Micro kit (Ambion) or RNeasy micro kit (QIAGEN) was used. cDNA was generated by using iScript cDNA synthesis kit (Bio-Rad). qPCR was performed based on SYBR green method using SYBR green/Rox PCR Master Mix (Kapa Biosystems). In some cases, qPCR was performed with Taqman method using gene-specific probes (ABI Applied Biosystems). All qPCR reactions were carried out according to manufacturer's suggestions on ABI StepOnePlus real-time PCR system. Relative levels of cDNA for the interest genes were normalized with the level of those of Glyceraldehyde-3-Phosphate Dehydrogenase (GAPDH) or M-CSF receptor (CSF1R) (when myeloid cells are concerned) in the same cDNA templates. The detailed primer sequences (for SYBR qPCR) and Taqman probes can be found in the [Key Resources Table](#).

### Immunofluorescence staining and image processing

In brief (Liu et al., 2011), mice were anaesthetized (60mg/kg ketamine; 12 mg/kg xylazine) and perfused through the right cardiac ventricle with PBS, followed by 4% paraformaldehyde (PFA). Brains were then post-fixed overnight at 4°C, cryoprotected in 30% sucrose (two days at 4°C) and embedded into optimal cutting temperature (O.C.T.) prior to cryo-sectioning on a cryostat. 12-20 µm sections were captured onto plus slides and dried at room temperature for 1 hour. Tissue slices were then rehydrated with PBS, blocked in 10% serum in PBST (PBS + 0.3%–0.5% Triton X) for 1 hour at room temperature and incubated with primary antibodies (diluted in 1% serum PBST) overnight at 4°C. After several washes, Alexa dye conjugated secondary antibodies (Life Technologies) were applied at 1:500 for 2 hours at room temperature. Following several washes with PBS and counterstaining with DAPI, tissue slices were mounted in 70% glycerol with coverslips. Primary antibodies used were listed below: GFP (Chicken, Aves Labs), IBA1 (Rabbit, DAKO or Goat, Abcam), P2ry12 (Rabbit, Abcam), TMEM119 (Rabbit, Abcam), GFAP (Rabbit, DAKO), PDGFRα (Goat, R&D), NeuN (Rabbit, Abcam), ER-TR7 (Rat, Abcam). To perform CD3e (Armenian Hamster, eBioscience) staining, spleen and tumor tissues were dissected out without perfusion and fixed with 4% PFA at room temperature for one hour. We used BrdU incorporation method to identify proliferating cells (Wojtowicz and Kee, 2006). Mice were first intraperitoneally injected with BrdU (50 mg/kg) prior to



perfusion. To visualize incorporated BrdU in cells/tissues, slices were pre-treated with 2M HCL to denature the DNAs and expose BrdU incorporated regions for BrdU antibody (Rat, Bio-rad) to bind.

Images were acquired on confocal system (Zeiss LSM700 or Zeiss LSM880) and processed using ImageJ or Adobe Photoshop CS 6.0 (San Jose, CA). Morphology of Microglia and TAMs was traced by NeuroLucida software (Nikon).

### Quantification of TME cells throughout tumor development

Tissue sections from  $\geq 3$  mice at 3 distinct stages (early, mid, late) of tumor development were immunostained for GFP/RFP fluorescent proteins, CD31 to visualize blood vessels, IBA-1 to visualize microglia/macrophages, BLBP to visualize astrocyte cell bodies, and DAPI for all nuclei. Since medulloblastoma originates from granular neuron precursors (GNPs) in the external germinal layer (EGL), we chose EGL rather than adult cerebellum as the control for comparison to tumor regions. We dissected cerebellum from postnatal day 6 (P6) pups, performed the immunofluorescence staining with the corresponding marker proteins as in tumors. Three images were taken per tumor/EGL at 200X magnification throughout the tumor/ P6 cerebellum. Due to ambiguity in determining individual tumor GNPs, given the dense cellularity of these tumors, DAPI was used as a proxy for total tumor cell number and in the EGL. Some TME cells will also be included in this number, but their presence is so low, compared to GFP+ tumor cells, that inclusion of these cells in total tumor cell number will not significantly affect interpretation. Blood vessel density was determined by quantifying the % area occupied by CD31+ signal. Microglia/macrophage numbers were determined by counting the number of IBA-1+ cells per field of view. Astrocyte numbers were determined by counting the number of BLBP+ cells per field of view. The percentage of TME cell population numbers was calculated by dividing the # of marker-positive cells by the # of total DAPI+ cells in the same field of view and multiplied by 100 to output a percentage value. ImageJ was used for image processing and counting. Excel and Graph Pad Prism were used to perform statistical analysis and a one-way ANOVA was applied to determine significance and error bars represent standard deviation.

### RNA *In situ* hybridization

Please refer all probes (IGF1 and IL4) for *in situ* hybridization to Allen Brain atlas. In brief (Zhao et al., 2009), DNA fragment amplified by PCR were ligated into pGEMT-easy vector. The plasmids containing the relevant DNA fragment were purified and then linearized by restriction enzyme. The linearized plasmids were used as template to generate labeled RNA probes with Digoxin by transcription *in vitro* (Roche). RNA probes (1  $\mu\text{g}/\text{ml}$ ) were hybridized with cryosectioned slices (12  $\mu\text{m}$ ) at 64°C overnight. BCIP/NBT substrates were used to visualize the hybridized cells/tissues. Immunofluorescence staining was carried out after hybridization if we need to pinpoint the particular cell types with positive RNA hybridization signals. In that case, the hybridized slides were further fixed with 4% paraformaldehyde (PFA) for fifteen minutes at room temperature, blocked with 5% donkey serum for one hour at room temperature, followed by primary (IBA, Ki67 and GFAP) and secondary antibody incubation at 4°C overnight. The nuclei were counterstained with DAPI (4', 6-diamidino-2-phenylindole). At least three tumors were analyzed. Images were acquired from Olympus fluorescence microscope and processed by imageJ.

### Fluorescent *In Situ* Hybridization of chromosome loci with immunofluorescence

Tissue microarray (TMA) paraffin sections were mounted on silanized slides, baked for 5 minutes at 90°C, and then de-paraffinized in xylene. Slides were briefly dehydrated in 100% ethanol followed by 35 minutes in hot 1 mM EDTA. Sections were rinsed in dH<sub>2</sub>O and incubated with GFAP (Abcam) diluted in CAS Block (Invitrogen Corporation). Slides were washed in 1X PBS and then incubated with FITC conjugated fluorescent secondary antibody (Abcam) diluted in CAS Block. There is an additional wash in 1XPBS followed by fixation in 4% paraformaldehyde (USB Corporation) for 20 minutes. Slides were dehydrated in an ethanol series and air-dried. 20  $\mu\text{l}$  of PTCH1/CEP9 (with GFAP) probe working solution (Empire genomics) was applied to the hybridization area, a 24x50 mm coverslip is placed over the top, and the edges of the coverslip were sealed with a continuous bead of rubber cement. The slide and probe were co-denatured at 95°C for 4 minutes and hybridized 24 hours or more at 37°C in a humidified chamber. Slides were then washed in 2X saline sodium citrate buffer (SSC)/0.1%NP40 at 70°C for 1 minute and DAPI counterstain (Vector Laboratories) was applied as well as a glass coverslip. Visualization of the dual FISH/immunofluorescence signals was accomplished by use of a fluorescent microscope with standard filters.

### Laser Capture Microdissection

We chose GFP-guided single cell Laser Capture Microdissection over tissue dissociation considering that non-physiological noises at transcription level could occur during tissue dissociation. For example, an immune signature would be hard to interpret because it is known that glia cells tend to get into an “activated” state after going through a dissociation process (Bennett et al., 2016).

The laser capture microdissection (LCM) experiment was designed and modified according to previous studies (Janes et al., 2010; Wang and Janes, 2013). Briefly, tumor brains were removed and slowly lowered into liquid nitrogen-cooled methyl-butane. The brains were kept fully submerged for 1 minute then store at  $-80^{\circ}\text{C}$ . Tumor brain was cut at 8  $\mu\text{m}$  thickness on a cryostat and sections were collected on positively-charged slides. Slides were fixed in 100% ethanol for 5 minutes at room temperature and then transferred into 100% xylene for 5 minutes at room temperature. Slide was then air-dried for 5 minutes. Laser capture microdissection of individual cells was performed on an ArcturusXT LCM system (Applied Biosystems) with an infrared laser using CapSure HS LCM caps after optimization of laser power and duration.

Since paraformaldehyde fixation would negatively affect the RNA quality and the subsequent sequencing, all samples were snap frozen without fixation. We found that GFP molecules quickly diffuse away from labeled cells once tissue sections melt or encounter moisture. After extensive troubleshooting we found that pre-chilling slides in the cryostat could prevent melting once tissue sections

touch the slide. This trick gave us a couple of precious seconds to dip the slide with still-frozen sections into ethanol to not only fix the RNA but also remove water from sections to prevent GFP loss.

We sectioned the tissue at 8  $\mu\text{m}$  to minimize contamination from the z axis. Initially we tried to use UV laser and found that single cell cutting with UV laser completely destroyed RNAs in the cell, most likely due to the high energy level of UV laser. When we switched to lower-energy IR laser that melts a small point of wax onto each target cell to pull it off, we found that the strength of attachment of sections to slides needs to be optimized every time for precise cell collection. If they attached too loosely, the IR laser would pull off too many surrounding tissue with the target cells. On the other hand, if tissue sections attached too tightly, the IR laser would fail to pick up individual target cells into the collection cap. We controlled the attachment strength by warming up pre-chilled slides for  $\sim 1$  s (touch finger tip under the slide) then immediately proceeded to LCM. If we encountered problems, the time could be lengthened slightly to increase attachment strength, or shortened slightly to reduce it.

### **RNA extraction, cDNA amplification, library construction and RNA sequencing of LCM micro-dissected tissues/cells**

RNA extraction and cDNA amplification procedures were performed as described under optimized conditions for 50 microdissected cells. For each sample, 250 cells were microdissected per LCM cap and split into five 50-cell technical replicates (as a control, one replicate did not undergo reverse transcription) after elution from the cap. Reamplified cDNA ( $\sim 500$  bp 3' ends) was purified away from primer concatemers by two rounds of purification with 0.7  $\times$  volume of AMPure XP beads (Beckman) according to the manufacturer's recommendations, and purified cDNA was quantified by Qubit assay (Life Technologies). For each sample, 1 ng was tagged with the Nextera XT kit (Illumina) and sequenced as 75 bp paired-end reads on a NextSeq instrument using v2 reagents (Illumina). 14–22 million reads per sample were filtered for signal to noise (chastity filtered), assessed for overall quality with FastQC (<http://www.bioinformatics.babraham.ac.uk/projects/fastqc/>), and then mapped with STAR (Dobin et al., 2013) against the mouse genome build mm10. Data were quantified as reads per million (RPM), and  $\log(\text{RPM}+1)$  values were clustered hierarchically in MATLAB after row standardization with a Euclidean distance metric and Ward's linkage.

### **Primary tumor GNP purification and *in vitro* culture**

Primary tumor GNPs were purified with percoll gradient method (Lee et al., 2009). In brief, tumor mice were anaesthetized (60mg/kg ketamine; 12 mg/kg xylazine) and tumor tissues were dissected out and digested with Papain (Worthington Biochemical) for 45 minutes at room temperature. Digested tumor pieces were then triturated into single cell dissociates and cleared by passing through 70 $\mu\text{m}$  cell strainer. The cleared dissociates were applied to percoll gradient (35%/65%) followed by centrifugation at 1300 g for 30 minutes. The cells located at the interface of these two gradient layers are mainly tumor GNPs. These cells were carefully collected and transferred into a new polystyrene tube, washed and spun down at 1000 g for 5 minutes. To evaluate the effects of growth factors (such as IGF1 and HGF),  $1 \times 10^5$  cells were seeded onto PDL pre-coated coverslips in Neurobasal media supplemented with B27 minus insulin. 4 hours post seeding, IGF1 or HGF was added at varying concentrations. After 2 days in culture, EdU was added at 0.1mM for 3 hours prior to cell harvesting. The proliferation of tumor GNPs was evaluated by EdU incorporation. All experiments were repeated at least three times. Images were acquired on Olympus fluorescence microscope and processed by ImageJ program.

### **Isolation of primary Tumor Associated Microglia/Macrophages (TAMs)**

This purification method was adapted from adult microglia purification method (Nikodemova and Watters, 2012). All steps were performed on ice whenever possible. To get rid of circulating immune cells from brain/tumor tissues, mice underwent trans-cardiac perfusion with sterile ice-cold PBS before tumors were dissected out. Dissected out tumor pieces were digested with Papain (Worthington Biochemical) at 37°C for 45 minutes and dissociated by trituration. Tissue debris was removed by passing tumor dissociates through a 70 $\mu\text{m}$  cell strainer. Cleared tumor dissociates were then applied to Percoll gradient (18.6%/62.5%) centrifugation at 1300 g for 30 minutes to get rid of myelin and cell debris. The cells that were collected from interface between 18.6% and 62.5% Percoll layers were then captured by anti-CD11b magnetic beads (Meltiny Biotec, Germany) to enrich tumor associated CD11b+ myeloid populations (TAMs). Finally TAMs were separated out in a magnetic field using MS columns (Meltiny Biotec, Germany) or through autoMACS Pro Separator.

### **Co-culture of TAMs with Tumor GNPs**

TAMs were isolated as described above. To ensure the sterility during culture, after trans-cardiac perfusion, tumor mouse was decapitated and soaked completely in betadine before the tumor pieces were dissected out. Also in the final step of TAMs purification, TAMs were manually separated out through MS columns in a laminar hood. The viability of TAMs were evaluated by Trypan blue staining and cell counting under the microscope based on dye exclusion. We consistently reached more than 90% viability. The purity was assessed by counting the contaminated Math1-GFP+ tumor cells and by Iba1 staining. Usually we have less than 10% tumor cell contaminated and Iba1+ cells are approximately 90%. To set up co-culture with tumor cells, acutely prepared TAMs were seeded up to 10K onto coverslips and cultured in Neurobasal media supplemented with B27 (Life Technologies) and 10ng/ml M-CSF (Peprotech) overnight to recover. Next day, TAMs were washed twice with D-PBS. GFP+ tumor GNPs were seeded on top of TAMs at 100K in Neurobasal media supplemented with B27 minus insulin and 5ng/ml M-CSF. After 2 days in culture, EdU was added at 0.1mM for 3 hours prior to cell harvesting. The proliferation of GFP+ tumor GNPs was evaluated by EdU incorporation.

### Flow cytometry

Immune cells were isolated from tumors as described above. After percoll gradient centrifugation, myelin-free cell suspension was incubated with anti-CD45 magnetic beads (Meltinyl Biotec, Germany) at 4°C for 15 minutes to capture all immune cells in the tumors. All the tumor associated immune cells (CD45+) were then separated out through autoMACS Pro Separator. To pin down the identities of these immune cells, surface marker staining followed by flow cytometry was performed with these immune cells. All the staining procedures were carried out at 4°C and in PBS with 0.5% BSA+ 2mM EDTA to maximize the cell viability. To reduce the non-specific immunofluorescence staining, the cells were pre-incubated with anti-mouse CD16/32, a Fc receptor blocker (eBioscience) for 10 minutes. Then the cells were incubated in an antibody cocktail consisting BV421 anti-CD11b, APC anti-CD45 (BD Bioscience), PE-Cy7 anti-CD19, PE anti-CD3e (eBioscience), biotinylated anti-NK1.1, Zombie Aqua Live/dead dye (BioLegend) for 30 minutes. Cells were then washed with PBS/0.5%BSA/2mM EDTA, and centrifuged at 350 g for 10 minutes at 4°C. Pellets were re-suspended and incubated with BV605 conjugated streptavidin for 30 minutes, followed by centrifugation at 350 g for 10 minutes at 4°C. Cell pellets were re-suspended in PBS and proceed for flow analysis. In a separate analysis of myeloid cell surface markers, the cells were pre-incubated with anti-mouse CD16/32, a Fc receptor blocker (eBioscience) for 10 minutes. Then anti-P2ry12 (AnaSpec, rabbit polyclonal) was added at 1:400 and incubated for 30 minutes. Cells were washed with PBS/0.5%BSA/2mM EDTA, and centrifuged at 350 g for 10 minutes at 4°C. Pellets were re-suspended in an antibody cocktail consisting BV421 anti-CD11b (BD Bioscience), 647 anti-CD192 (CCR2), BV605 anti-CD11c, PE-Cy7 anti-CD45, Zombie Aqua Live/dead dye (BioLegend), PE goat anti-rabbit secondary antibody (ThermoFisher Scientific) and incubated for 30 minutes, followed by centrifugation at 350 g for 10 minutes at 4°C. Cell pellets were re-suspended in PBS and proceed for flow analysis with BD LSRFortessa cytometer. Data were analyzed with FlowJo v10 software.

### RNaseq and data analysis of TAMs

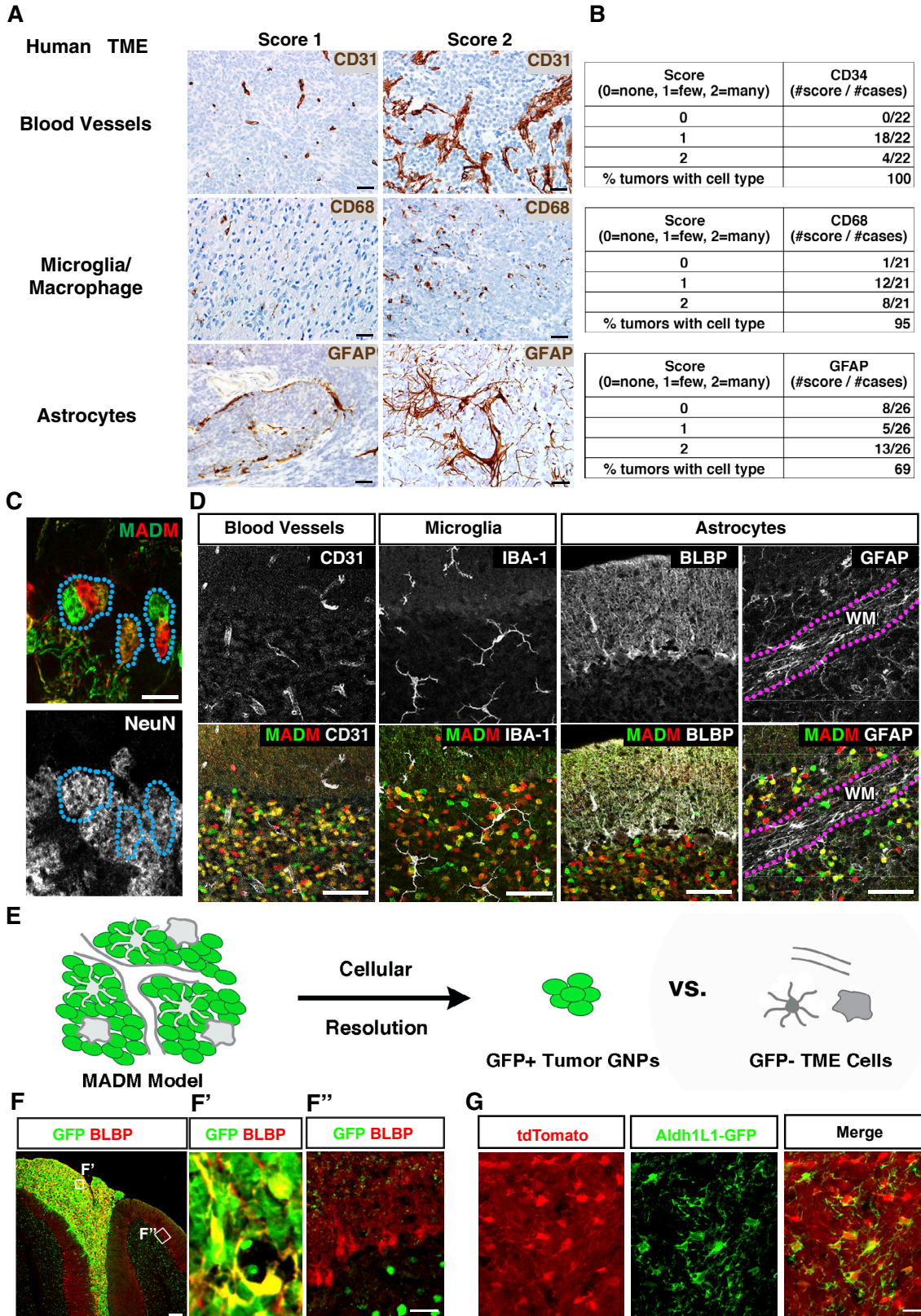
Total RNAs of TAMs and normal microglia from age matched mice were extracted using the RNeasy micro kit (QIAGEN) according to manufacturer's protocol. RNA Quality was assessed by Bioanalyzer (Agilent Technologies) and samples with RNA integrity > 8 were used for library construction. First and second-strand cDNA synthesis, RNaseq library construction and sequencing were carried out by BGI Americas. High-quality libraries were sequenced by the Illumina® Hiseq2500 sequencer to obtain 75bp paired-end reads. Reads alignment to mm10 mouse reference genome, data processing and TPM (Total read per million) calculation were done by using package in the R statistical computing environment (Anders and Huber, 2010; Patro et al., 2014; Soneson et al., 2015). After estimating transcript abundances with Sailfish (Patro et al., 2014), we converted the abundance estimates to counts of reads mapping to GENCODE genes using the tximport package in the R statistical computing environment (Sonesson et al., 2015). We then used the DESeq2 Bioconductor package (Love et al., 2014) to normalize count data, estimate dispersion, and fit a negative binomial model for each gene. GENCODE/Ensembl gene IDs mapping to predicted genes were excluded and the Benjamini-Hochberg False Discovery Rate procedure was used to re-estimate the adjusted p values for GENCODE/Ensembl gene IDs mapping to known genes. Genes were filtered for low abundance by selecting on genes with a TPM > 20 in at least one group. Pathway analyses were performed using a compilation of previously defined pathways from consortiums such as GO via the Broad Institute's MSigDB resource (Subramanian source). Fisher's exact tests were performed to determine significant pathway enrichment. All codes used for analyses are available upon request.

### QUANTIFICATION AND STATISTICAL ANALYSIS

Statistical significance was determined using GraphPad Prism 6 using unpaired Student's two-tailed t test, one-way ANOVA or two-way ANOVA, according to test requirements. No inclusion/exclusion criteria were pre-established. Grubbs' Outlier Test was used to determine outliers, which were excluded from final analysis. A P value of < 0.05 (indicated by one asterisk), < 0.01 (indicated by two asterisks), < 0.001 (indicated by three asterisks), < 0.0001 (indicated by four asterisks) or were considered significant.

### DATA AND CODE AVAILABILITY

RNA-sequencing data of TuAstrocyte were deposited in Gene Expression Omnibus (GEO): GSE111734. RNA-sequencing data of TAMs were deposited in GEO: GSE109750. This study did not generate any unique code.



---

**Figure S1. TME Cells in Medulloblastoma and Characterization of *Math1-Cre*, Related to Figure 1**

(A) Representative images and the scoring scheme for TME cell composition in human SHH-subtype medulloblastoma samples.

(B) Data summary of TME cell composition from (A).

(C) In adult MADM-WT mice, only NeuN<sup>+</sup> granule neurons in IGL were labeled, demonstrating the faithful expression of *Math1-Cre* in GNPs.

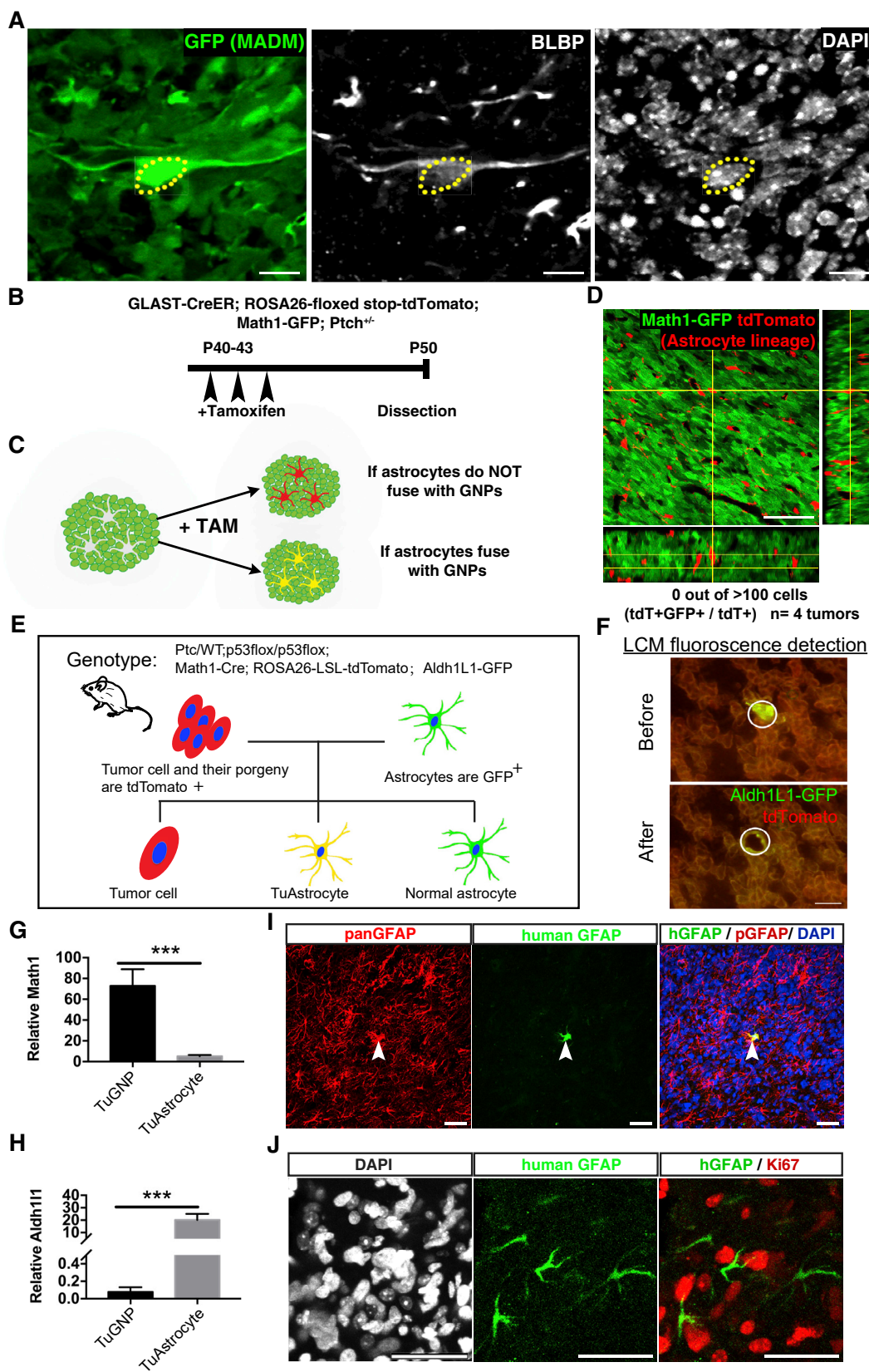
(D) There was no MADM labeling of potential TME cells, including blood vessels (CD31), microglia (IBA-1), and astrocytes (BLBP, GFAP).

(E) In the MADM model, tumor GNPs are GFP<sup>+</sup> while TME cells are expected to be unlabelled, allowing cellular resolution analyses of tumor-TME interactions from tumor initiation throughout progression.

(F) GFP<sup>+</sup> astrocytes are present only in tumors (F'), but never in tumor-free brain regions (F''). G, A mouse medulloblastoma model in which all cells from GNP lineage is tdTomato<sup>+</sup> while astrocytes are labeled by Aldh1L1-GFP. If tumor-associated astrocytes were derived from tumor cells, they should be yellow (Aldh1L1-GFP<sup>+</sup> and tdTomato<sup>+</sup>).

[WM = White matter].

Scale bars: (A), (D), and (F), 50  $\mu$ m; (F') and (F''), 10  $\mu$ m; (G), 25  $\mu$ m.



(legend on next page)

---

**Figure S2. Validation of Tumor-to-Astrocyte *trans*-Differentiation with Multiple Approaches, Related to Figure 2**

(A) BLBP<sup>+</sup> tumor-associated astrocytes had only one nucleus (representative image of > 100 cells/tumor in 10 tumors), suggesting that GFP-labeling of astrocyte-like cells did not result from cell fusion.

(B–D) Mouse model and tamoxifen dosing scheme (B), experimental outcome predictions (C), and a representative image (D) of a mouse medulloblastoma model, in which astrocytes were labeled with tdTomato following the excision of the “floxed stop cassette” by *GLAST-CreER* upon tamoxifen injection, while TuGNPs were labeled by *Math1-GFP*. The fact that none of the tdTomato-labeled cells expressed GFP suggests that cell fusion did not occur.

(E) Tumor-associated astrocytes were labeled with *Aldh1L1-GFP* in a medulloblastoma model in which tumor lineage is labeled with tdTomato. This enables distinction of tumor-associated astrocytes (yellow) from normal astrocytes (green) and tumor GNPs (red).

(F) Circled region indicated one micro-dissected tumor-associated astrocyte with minimal contamination of neighboring cells. The gamma scaling in the GFP channel was adjusted to 0.5 to highlight GFP fluorescence clearly above tissue autofluorescence.

(G–H) Purity verification of LCM-dissected tumor-associated astrocytes versus TuGNPs before RNA-sequencing. qRT-PCR showed minimal *Math1* expression (*Math1*: 72.92 ± 16.01 TuGNPs versus 5.252 ± 1.13 tumor-derived astrocytes,  $p = 0.0002$  t test,  $n = 4$ ) and strong enrichment of *Aldh1L1* expression (*Aldh1L1*: 0.078 ± 0.053 TuGNPs versus 20.15 ± 4.892 TuAstrocytes,  $p = 0.0002$  t test,  $n = 4$ ) in the tumor-derived astrocytes pool.

(I) Anti-human GFAP antibody specifically labels human astrocytes (arrowhead) in mouse brain grafted with human medulloblastoma cells (DAPI in blue labels all cell nuclei).

(J) Serially xenografted SHH-subtype human medulloblastoma cells (passage 12 shown here) gave rise to sporadic cells with astrocytic morphology that stained positive for human GFAP protein throughout the tumor mass, suggesting *trans*-differentiating activity of human medulloblastoma cells could be maintained in the long-term.

[*GLAST* = glutamate transporter],

Scale bars: (A), 10 μm; (F), 20 μm; (D), (I), and (J), 50 μm. Data are Means ± SD. Student's t test. n.s.: not significant; \*\*\* $p < 0.001$ .

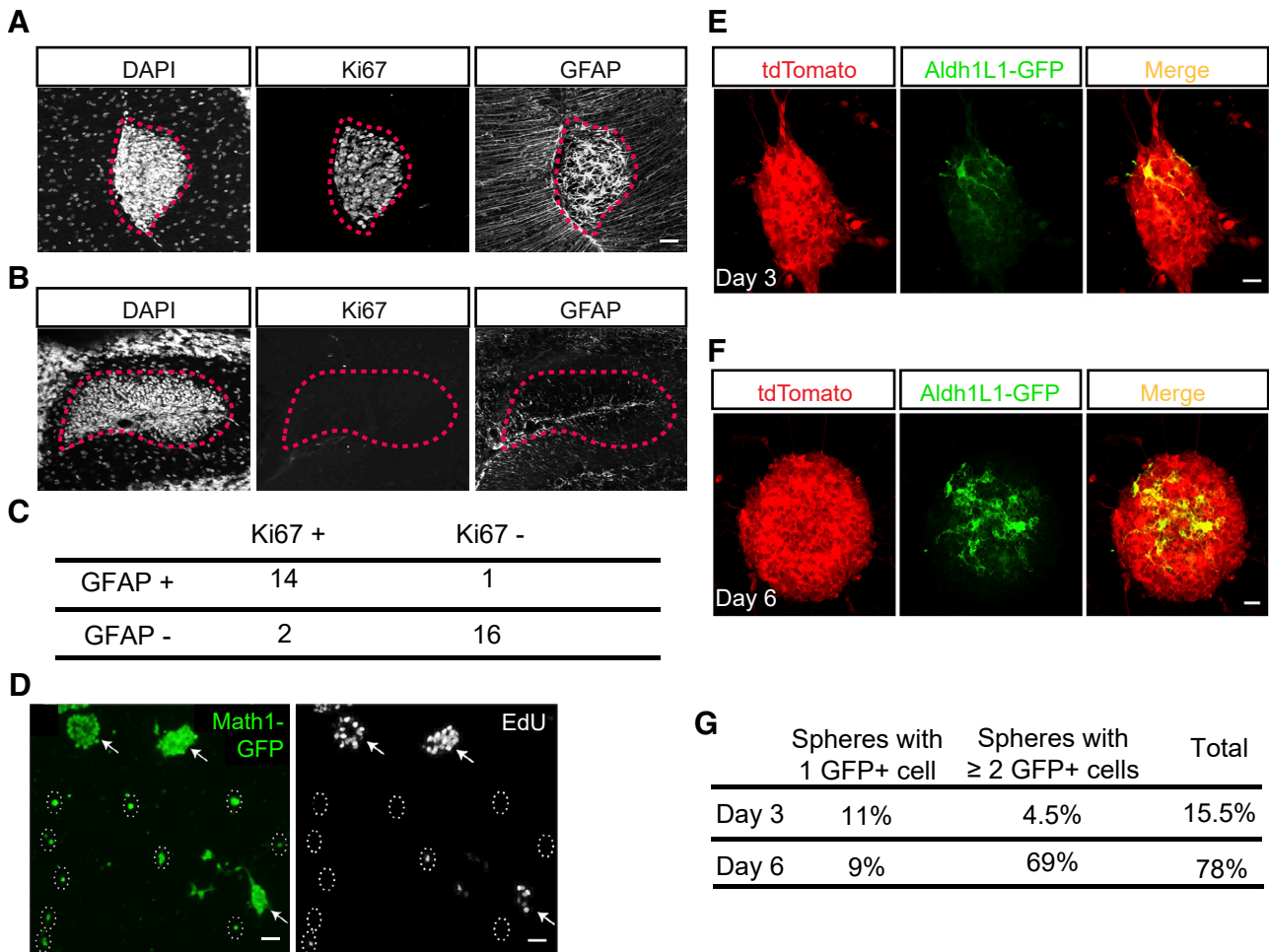


**Figure S3. Supportive Role of TuAstrocytes in Medulloblastoma Progression, Related to Figure 3**

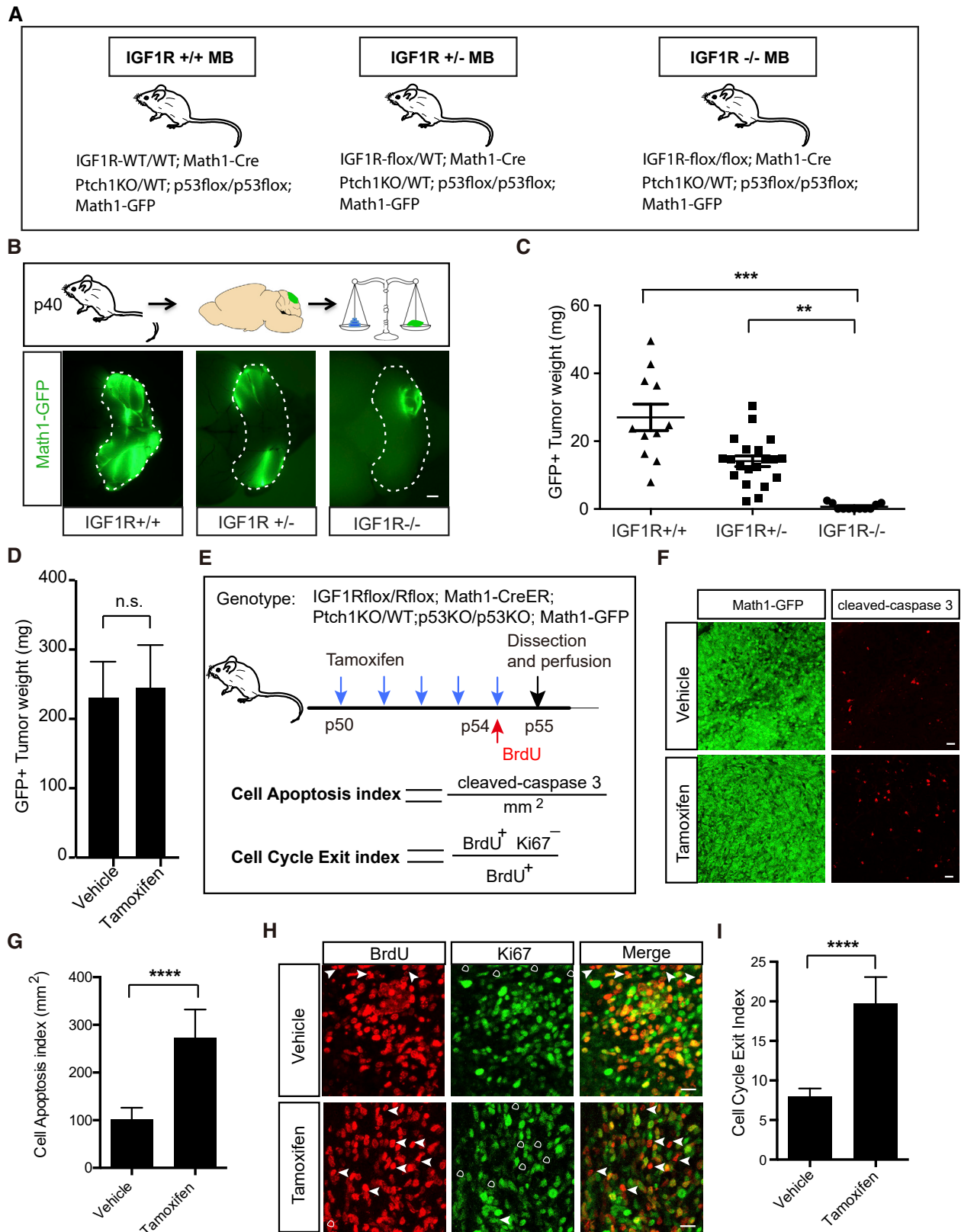
(A–C), In PNLs, the proliferation of TuGNPs strongly correlated with the presence of TuAstrocytes.

(D), TuGNPs (Math1-GFP<sup>+</sup>) proliferated actively (EdU<sup>+</sup>) in spheres (arrows) but not as dispersed cells (circled).

(E–G), TuAstrocytes (Aldh1L1-GFP<sup>+</sup>) gradually appeared in tumor spheres.

Scale bars: (A), (B), (D), (E), and (F), 50 μm.





---

**Figure S4. Inactivation of the IGF1R in GNPs Delays Tumor Progression, Related to Figure 4**

(A) Medulloblastoma mouse model with IGF1R knockout in GNPs.

(B) Mice with different genotypes (IGF1R<sup>-/-</sup>; IGF1R<sup>-/+</sup>; IGF1R<sup>+/+</sup>) were dissected at postnatal day 40 and tumor tissues (Math1-GFP<sup>+</sup>) were collected and weighted. Dotted line indicates cerebellum area.

(C) Graph of tumor weight from tumor mice of different genotypes: IGF1R<sup>-/-</sup> (n = 14), IGF1R<sup>-/+</sup> (n = 20) and IGF1R<sup>+/+</sup> (n = 11).

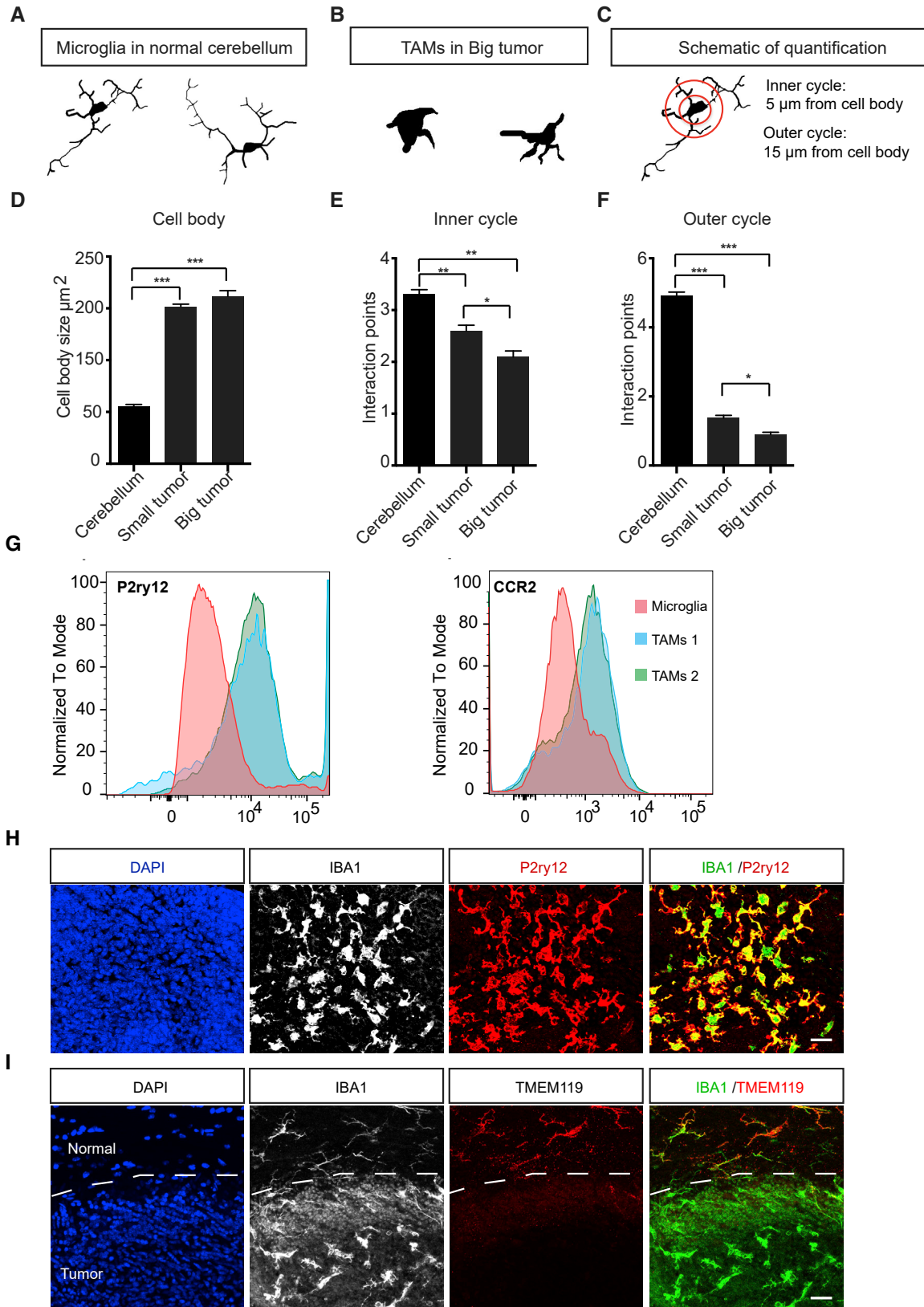
(D) Tamoxifen (150 mg/kg) did not affect tumor progression in comparison to vehicle control. n = 10 for each group.

(E) Schematic illustration on IGF1R inactivation in tumor cells. After 5 pulse Tamoxifen gavage, the tumor was harvested and apoptotic index and cell cycle exit index were quantified in tissue sections.

(F–G) Elevated apoptotic cells in Tamoxifen-treated group in comparison to vehicle group.

(H–I) There were more cells that exited cell cycle (BrdU<sup>+</sup>Ki67<sup>-</sup>) in Tamoxifen-treated group in comparison to vehicle group.

Scale bars: (B), 1mm; (F) and (H), 20  $\mu$ m. Data are Means  $\pm$  SD, one-way ANOVA (C) or Student's t test (D G and I). n.s.: not significant, \*p < 0.05; \*\*p < 0.01; \*\*\*p < 0.001.



---

**Figure S5. TAMs Display Activated Morphology and Express Cell Markers of Both Microglia and Monocyte-Derived Macrophages, Related to Figure 5**

(A and B) Morphologies of TAMs were traced by neurolucida program in big tumors (B), in comparison to microglia in normal cerebellum (A).

(C) Schematic diagram of branching pattern analysis.

(D–F), Morphological analysis of microglia versus TAMs showed that TAMs had enlarged cell bodies (D) and shortened processes (E and F) in comparison to normal microglia. n = 213 normal microglia and 288 TAMs from 5 tumor mice.

(G) Flow-cytometry analysis showed that TAMs expressed both microglia marker (p2ry12) and macrophage marker (CCR2).

(H) Immunofluorescent staining of P2ry12 (red, microglia specific marker) and IBA1 (green, pan-microglia/macrophage marker) showed that TAMs expressed P2ry12.

(I) Immunofluorescent staining of TMEM119 (red, microglia specific marker) and IBA1 (green, pan-microglia/macrophage marker) showed that TAMs were TMEM119<sup>-</sup> while normal microglia were TMEM119<sup>+</sup>.

Scale bars: (H) and (I), 30 $\mu$ m. Data are Means  $\pm$  SD, one-way ANOVA. n.s.: not significant, \*p < 0.05; \*\*p < 0.01; \*\*\*p < 0.001.

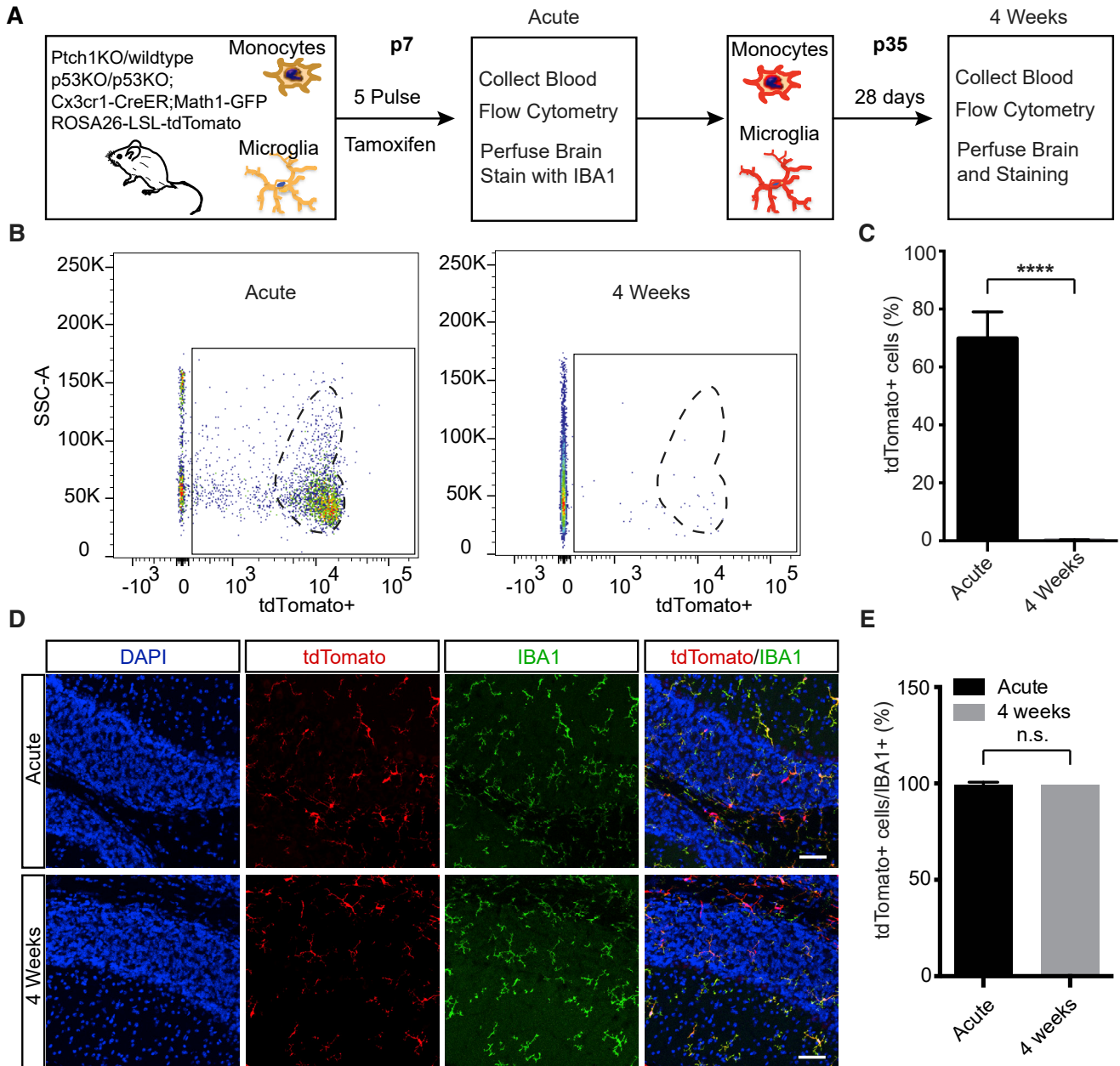


**Figure S6. Validation of the Lineage Tracing Genetic Tool to Differentiate Microglia from Circulating Monocytes in the Medulloblastoma Model, Related to Figure 6**

(A) Schematic diagram of the tool validation: In brief, pups were subcutaneously injected with Tamoxifen (50 mg/kg) at postnatal day four to day eight, *long before tumor initiation*. One day (acute) or Twenty-eight days (4 weeks) after injection, peripheral blood cells were collected for flow analysis and brains were collected for immunofluorescence staining.

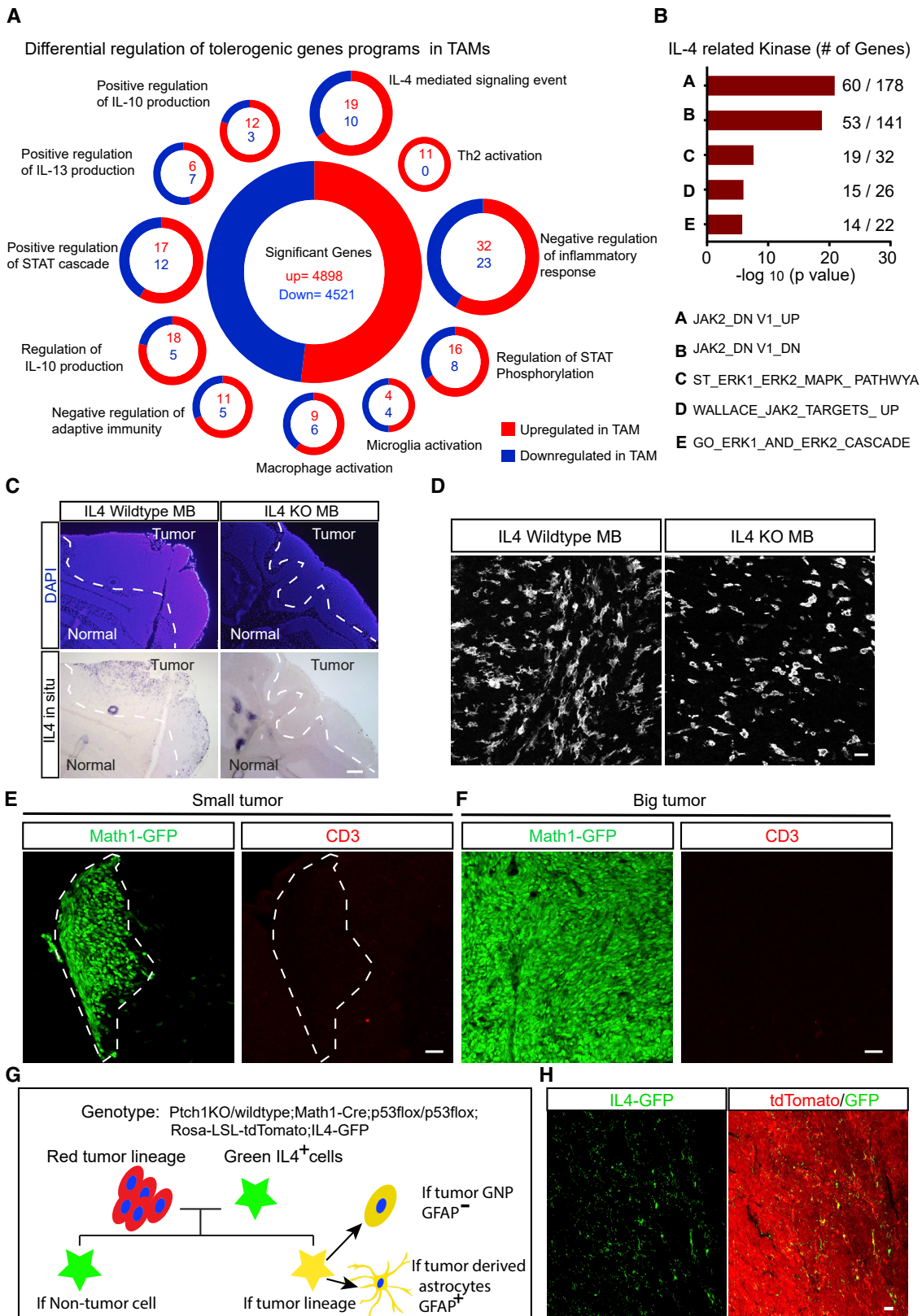
(B) Histogram of flow analysis of tdTomato<sup>+</sup> cells in the peripheral blood showed that tdTomato-labeled cells at acute phase were turned over by 4 weeks (still long before tumor formation).

(C) Quantification of flow analysis of tdTomato<sup>+</sup> cells in the peripheral blood.

(D) Immunofluorescent staining showed that all microglia (IBA1<sup>+</sup>, green) were tdTomato<sup>+</sup> (red) in both acute and 4 weeks group.

(E) Quantification from immunofluorescent staining showed that microglia had rare turnover in the cerebellum.

Scale bar: (D), 30 $\mu$ m. n = 5 mice for each group. Data are Means  $\pm$  SD, Student's t test. n.s.: not significant; \*\*\*\*p < 0.0001.



(legend on next page)

---

**Figure S7. IL-4 Produced by TuAstrocytes Activates TAMs, Related to Figure 7**

(A) TAMs exhibited robust tolerogenic gene program expression. Pathway analysis of the significantly up- and downregulated transcripts in tumor-associated microglia (focusing on immune signatures) revealed robust differential expression of genes associated with IL-4 signaling, IL-10 production, regulation of adaptive immunity, and macrophage/microglia activation. Shown in red were the significantly upregulated genes in tumor associated microglia relative to normal microglia from age-matched mice, whereas blue denoted downregulated genes. Immune signature genes were pulled from the MSigDB database.

(B) We observed significantly differentially regulated gene signatures associated with additional IL-4/STAT6 signaling components, JAK2 and ERK1/ERK2. Shown is the level of significance of a given pathway (the negative log of the p value) as well as the number of significantly differentially expressed genes in a given pathway over the total number of genes reported in that pathway. P values were determined using Fisher's exact tests. n = 5 tumor mice for RNaseq.

(C) *In situ* hybridization showed that IL4 mRNA could not be detected in IL4 KO tumor mice, validating the effectiveness of gene KO.

(D) Immunofluorescent staining of IBA1 showed that the cell density of TAMs was similar between IL4 wild-type and IL4 KO tumors.

(E and F) Immunofluorescent staining of CD3 shows that there were no detectable T cells in the tumor mass.

(G) Schematic diagram of how to use a medulloblastoma model containing both IL4-GFP reporter and tdTomato tumor lineage marker to investigate the identity of IL4-producing cells.

(H) IL4-GFP overlapped with GFAP and tdTomato staining in the tumor mass, suggesting that IL4 was produced by tumor-derived astrocytes. n = 3 tumor mice (at least) for each panel.

Scale bars: (C) = 200  $\mu$ m, (D), (E) (F), and (H), 20  $\mu$ m. Data are Means  $\pm$  SEM, Student's t test. \*p < 0.05. n.s.: not significant, \*p < 0.01. \*\*p < 0.001.